Gas-particle flows in a microscale shock tube and collection efficiency in the jet impingement on a permeable surface

Omid Ejtehadi (امید اجتهادی)[1,2], Tapan K. Mankodi (तपन के मंकोड़ी)[3], Ilyoup Sohn (손일엽)[4], Byoung Jae Kim (김병재)[2], R. S. Myong (명노신)[5]

[1] Institute for Materials and Processes, School of Engineering, University of Edinburgh, Sanderson Building, King's Buildings Robert Stevenson Road, Edinburgh, EH9 3FB, UK

[2] School of Mechanical Engineering, Chungnam National University, 99 Daehak-ro, Yuseong-gu, Daejeon 34134, Republic of Korea

[3] Department of Mechanical Engineering, Indian Institute of Technology Guwahati, Guwahati, India

[4] Intelligent Simulation Center, Korea Institute of Science and Technology Information (KISTI), Daejeon 34141, Republic of Korea

[5] School of Mechanical and Aerospace Engineering, and ACTRC, Gyeongsang National University, Jinju, Gyeongnam 52828, Republic of Korea

Correspondence: myong@gnu.ac.kr (R. S. Myong); bjkim@cnu.ac.kr (B. J. Kim)

Abstracts: We investigate the flow physics of non-equilibrium gases in interaction with solid particles in a microscale shock tube and the collection efficiency in the jet impingement on a permeable surface. One interesting application of flows in shock tubes at low pressures or micro-shock tubes is needle-free injection technology where drug particles are delivered by shock waves. To investigate such problems, a new two-fluid model system coupled with second-order Boltzmann-Curtiss-based constitutive relationships for modeling a non-equilibrium gas was developed. We were specifically interested in how rarefaction affects the complex wave patterns observed in dusty gas flows and the role of bulk viscosity in diatomic and polyatomic gases exposed to moving shocks. Simulation results demonstrated how significantly the bulk viscosity can affect the topology of the solution in the Sod shock tube problem. Counter-intuitive flow features were noted, resulting from bulk viscosity effects and the incapability of the first-order theory, even when Stokes' hypothesis was abandoned (i.e., the Navier-Fourier model). After detailed analyses in one-, two-, and three-dimensional space for simplified flow problems, a case was designed to represent a needle-free injection device. In addition, a new concept of 'collection efficiency' was introduced that quantifies the efficiency of drug delivery in the two-phase jet impingement on the skin. We also derived a new 'vorticity transport equation' that takes the bulk viscosity and multiphase effects into account. Based on the new equation, the time evolution of vorticity growth rates was analyzed for all the contributing terms in the equation.

Keywords: Gas-particle flow; shock-particle interaction; microscale shock tube; needle-free injection; particle collection efficiency

I. INTRODUCTION

Studies of non-equilibrium effects on shock propagation in shock tubes were initially conducted to investigate shock attenuation in long tubes for tunnel and mine safety.[1, 2] However, over the past few decades, this topic has once again become important due to rapid advances in MEMS device fabrication techniques. Many MEMS applications exhibit shock wave propagation and interaction at sub-millimeter length scales, including wave-rotor compressors,[3] micro-propulsion technology,[4] shock-induced combustion in micro-engines,[5] and needle-free drug delivery.[6]

Rarefaction and wall effects are two key factors that govern the physics of flow in such channels. The investigation of rarefaction effects in a shock tube was pioneered by Duff[1] whose experiments revealed that a conventional shock tube operating at low initial pressures did not perform as predicted by theory. A reduction in shock speed due to the development of a laminar boundary layer behind the shock was reported. Other studies theoretically investigated the development of the boundary layer behind a shock[2, 7] and expanded on the attenuation of the shock wave due to rarefaction. Shock-wave deceleration and contact acceleration were also described by Mirels[2]. Roshko[8] provided theoretical relations for shock-processed gas distance and maximum flow duration time. The non-slip walls and constant shock strength assumptions are the main drawbacks of Roshko's model in microchannel studies.

While the analysis of shock waves on a macroscale is still an active area of research,[9-12] recently, various experimental[13-15] and numerical studies[16, 17] have been conducted to investigate the propagation and attenuation of shock waves in microscale channels. The one-dimensional numerical models of Mirshekari and Brouillette[18] and Ngomo *et al.*[19] suggested the potential disappearance of shock waves at sufficiently low-pressure ratios. Two-dimensional Navier-Stokes models in conjunction with slip and temperature jump boundary conditions were solved by Zeitoun and Burtschell[20] while Parisse *et al.*[21] investigated shock wave attenuation. Zeitoun *et al.*[22] approached the problem using Navier-Stokes, direct simulation Monte Carlo (DSMC), and Bhatnagar–Gross–Krook (BGK) equations for two different Knudsen (Kn) numbers (0.05 and 0.5) in planar channels and round tubes. Kumar *et al.*[23] analyzed the micro-shock tube problem in a two-dimensional axisymmetric configuration using the Navier-Stokes equation and velocity slip boundary condition and investigated rarefaction effects up to Knudsen numbers as high as 0.09. Watvisave *et al.*[24] investigated wall accommodation effects in micro-shock tubes by DSMC as well as a hybrid MD/DSMC

algorithm. They showed that the hybrid MD/DSMC method can capture local effects at the wall which cannot be captured using phenomenological gas-surface interaction models. Kai *et al.*[17] focused on shock formation and hot flow duration in tubes with propagation lengths more than one hundred times the diameter and showed that the conventional leaky piston model or any other numerical model failed to predict the microscale hot flow duration.

The aforementioned studies are of critical importance for the efficient design of devices that are based on flows inside a micro-shock tube. An important example of such apparatus is the needle-free drug delivery technology, which is used for vaccine/insulin delivery, gene therapy, and recently cosmetics industries.[25, 26] Non-invasive drug delivery methods can be categorized based on their particular design parameters, such as load, mechanism applied in the delivery of the load, site of delivery, and the working principles of the device. Apart from the intricacy that the microscale imposes, the presence of droplets or particles and their interaction with the shock waves can lead to further shock attenuation and the emergence of complex wave patterns[27-29] which adds to the complexity of the analysis.

In such devices, the drug (either in liquid or solid phase) is delivered by a high-velocity jet after the skin is microscopically punctured. Liquid jet injectors, initially proposed in the 1940s by Hingson and Hughes,[30] employ various mechanisms to obtain a high-speed jet. Examples include spring force, compressed gas, Lorentz actuators, voice coil, and pulsed lasers. Important factors that affect the stability and collimation of the jet from a needle-free drug delivery nozzle include exit velocity, total pressure drop, and boundary layer thickness. At the same time, gas-powered powder injection is finding its way into drug delivery technology because it provides advantages compared to the conventional approach and the liquid jet injectors discussed earlier. In this work, we focus on gas-powered powder injection systems, where a drug in the form of solid particles is propelled by shock waves. A summary of various types of non-invasive injection technologies plus a schematic of a shock-powered powder delivery device is provided in Fig. 1.

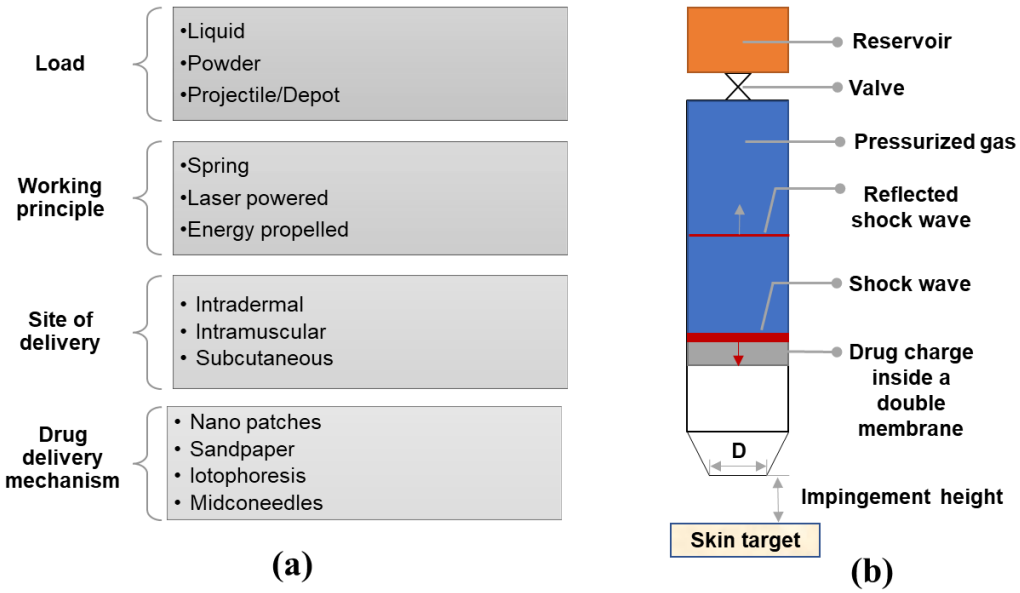

Fig. 1. (a) Categorization of various types of non-invasive injection technologies, (b) schematic of a shock-powered powder delivery device.

In such devices, the shock wave is produced by either application of a diaphragm or a controlled explosion. Because it is difficult to predict the proportion of dose that will be delivered to the epidermis, such systems are limited to those candidates with an effective dose of approximately 1 mg. There is also a 2 to 3 mg payload limitation for a 20 mm target area.

With this in mind, we aim to predict the sufficient density of powder particles for a range of therapeutic dose levels, and the acceleration required to reach velocities high enough to penetrate the skin. Various phenomena are involved in the simulation process, including shock wave attenuation, boundary layer formation, thermal non-equilibrium, and granular flows, which make the problem at hand a multifaceted one.

The numerical framework used in the present work was inspired by modeling the descent phase of the Lunar landing, where the plume of the descent engine causes erosion and hence entrainment of particles in the rarefied Lunar atmosphere.[31-33] In the current study, however, the non-equilibrium effects are due to the small scale of the geometry rather than the rarefaction effects. From a modeling point of view, apart from the non-equilibrium effects due to miniaturization, two-phase interactions between gas and solid particles add to the complexity of the problem, compared to a single-phase flow. The majority of the research in this category is based on the concept of transdermal injection suggested by Quinlan *et al.*[34] and Kendall *et al.*[35] who investigated a needle-free prototype. The operating conditions and the dimensions of

the device led to low-Knudsen and high-Reynolds regimes. This research was further extended through numerical simulations[36, 37] and experimental analysis.[38]

In the present study, a computationally efficient approach for predicting a two-phase flow in micro-shock tubes is first established. The non-negligible thermal non-equilibrium condition (measured by maximum Knudsen number 0.5 and maximum Mach number 1.6) is taken into account by applying thermodynamically consistent nonlinear coupled constitutive relationships (NCCR)[39-41] derived from the general hydrodynamics of Eu.[42-44] This model has been extensively studied in recent decades and has recently been extended to include new capabilities, such as the simulation of diatomic and polyatomic gases,[45] as well as the inclusion of vibrational degrees of freedom.[46] Using the developed approach we investigated non-equilibrium effects in micro-shock tubes up to relatively high Knudsen numbers in one-dimensional setups so that the rarefaction effects are the only relevant factor. The effect of the bulk viscosity of the gases for pseudo-diatomic gases is also studied in this paper. We then present the simulations in two and three-dimensional setups to include the wall effects besides the rarefaction effects. Also, the effect of added particles on the flow was investigated. This was done by elaborating on how rarefaction can affect the complex wave patterns observed in conventional dusty gas shock tubes.

Finally, the delivery of a particulate drug dose to the skin via a shock wave simulated in a simplified setup is presented. During the process, a new concept of 'collection efficiency' is introduced that quantifies the efficiency of drug delivery in the two-phase jet impingement on the skin. In addition, a new viscous compressible vorticity transport equation of two-phase flow including bulk viscosity is derived.

II. EULERIAN-EULERIAN MODELING OF A RAREFIED GAS AND SOLID PARTICLES

A. Two-fluid model equations for dusty gas flows

In the majority of two-fluid *Euler-Euler* models, as well as in the current study, for dusty gas flows, the gas phase is considered a compressible gas, which follows the perfect-gas law, while the solid phase is considered incompressible.[47-49] The inter-particle collisions are neglected, and the particles are assumed to be uniformly sized spheres with constant diameter, density, and temperature. As a result, the conservation laws for the solid phase do not include a pressure term. Additionally, it is assumed that the particle material's specific heat is constant.

Furthermore, the particles are also inert, and neither their thermal nor Brownian movements are taken into account. Moreover, the gravitational and buoyant forces, the effects of turbulence, and the impact of particle wakes are rendered insignificant.

On the other hand, in the *Euler-granular* models (as opposed to Euler-Euler), the solid pressure and viscous fluxes are retained for the solid phase to simulate granular flows.[50] In these two-fluid models, the number density of the particles should be large enough to avoid violating the continuum assumption. In the present study, an Euler-Euler approach is used as the volume fraction of the particles for most of the investigated cases is small.

Under the aforementioned conditions, the conservation laws (taking viscous effects and solid pressure into account) can be written as follows: for the gas phase,

$$\partial_t \mathbf{U}_g + \nabla \cdot \mathbf{F}_g = \mathbf{S}_g , \tag{1}$$

$$\mathbf{U}_g = \begin{bmatrix} \alpha_g \rho_g \\ \alpha_g \rho_g \mathbf{u}_g \\ \alpha_g \rho_g E_g \end{bmatrix}, \quad \mathbf{F}_g = \begin{bmatrix} \alpha_g \rho_g \mathbf{u}_g \\ \alpha_g \rho_g \mathbf{u}_g \mathbf{u}_g + p_g \mathbf{I} + \boldsymbol{\Pi}_g \\ (\alpha_g \rho_g E_g + p_g)\mathbf{u}_g + \boldsymbol{\Pi}_g \cdot \mathbf{u}_g + \mathbf{Q}_g \end{bmatrix},$$
$$\mathbf{S}_g = \begin{bmatrix} 0 \\ D_{g,s}(\mathbf{u}_s - \mathbf{u}_g) \\ D_{g,s}(\mathbf{u}_s - \mathbf{u}_g) \cdot \mathbf{u}_s + Q_{g,s}(T_s - T_g) \end{bmatrix}, \tag{2}$$

$$E_g = c_v T_g + \frac{1}{2}\left|\mathbf{u}_g\right|^2 , \tag{3}$$

and, for the solid phase,

$$\partial_t \mathbf{U}_s + \nabla \cdot \mathbf{F}_s = \mathbf{S}_s , \tag{4}$$

$$\mathbf{U}_s = \begin{bmatrix} \alpha_s \rho_s \\ \alpha_s \rho_s \mathbf{u}_s \\ \alpha_s \rho_s E_s \end{bmatrix}, \quad \mathbf{F}_s = \begin{bmatrix} \alpha_s \rho_s \mathbf{u}_s \\ \alpha_s \rho_s \mathbf{u}_s \mathbf{u}_s \\ (\alpha_s \rho_s E_s)\mathbf{u}_s \end{bmatrix},$$
$$\mathbf{S}_s = -\begin{bmatrix} 0 \\ D_{g,s}(\mathbf{u}_s - \mathbf{u}_g) \\ D_{g,s}(\mathbf{u}_s - \mathbf{u}_g) \cdot \mathbf{u}_s + Q_{g,s}(T_s - T_g) \end{bmatrix}, \tag{5}$$

$$E_s = c_m T_s + \frac{1}{2}\left|\mathbf{u}_s\right|^2, \tag{6}$$

$$\alpha_g + \alpha_s = 1. \tag{7}$$

Here the **U**, **F**, and **S** are the vectors of the conservative variables, fluxes, and source terms, respectively. The variables t, α, ρ, $\mathbf{u}$, E, p, T, $\mathbf{\Pi}$, and $\mathbf{Q}$ represent time, volume fraction, density, velocity vector, total energy, pressure, temperature, viscous stress tensor, and heat flux vector. Furthermore, c_v and c_m refer to the specific heat capacity of the gas at constant volume and the specific heat capacity of the particle material, respectively.

The terms $D_{g,s}$ and $Q_{g,s}$ in the source term vectors are the interfacial drag and heat transfer. The drag force that solid particles exert on the gas phase can be expressed as,

$$D_{g,s} = \frac{3}{4} C_D \frac{\alpha_s \rho_g}{d}\left|\mathbf{u}_g - \mathbf{u}_s\right|, \tag{8}$$

in which d is the particle diameter and C_D is the drag coefficient, usually computed as a function of the Reynolds number based on the particle diameter and relative velocity of the particle to the gas (i.e. $\mathrm{Re}_d = \frac{\rho_g d\left|\mathbf{u}_g - \mathbf{u}_s\right|}{\mu_g}$). Expressions which have included the effects of Mach and Kn numbers are also available in the literature.[51, 52] Studies on the application of proper drag models in dusty gas flows are available in the literature.[53] The comparison of models indicates that the tested models can produce almost identical results. Regarding the Mach number effects, as mentioned in Ben-Dor *et al.*[54], the application of incompressible drag coefficients for Mach numbers in the early supersonic regime is sufficient. Therefore, simple piecewise functions as provided by Dobran *et al.*[55] are applied in the current study:

$$C_D = \begin{cases} \frac{24}{\mathrm{Re}_d}\left(1 + 0.15\,\mathrm{Re}_d^{\,0.687}\right), & \text{if} \quad \mathrm{Re}_d < 1000 \\ 0.44, & \text{if} \quad \mathrm{Re}_d > 1000 \end{cases} \tag{9}$$

The heat transfer, which is proportional to temperature difference, can be expressed as a function of the Nusselt number,[56]

$$Q_{g,s} = \frac{6\mathrm{Nu}\kappa_g}{d^2}\alpha_s(T_g - T_s), \tag{10}$$

$$\mathrm{Nu} = 2 + 0.65\,\mathrm{Re}_d^{\frac{1}{2}}\,\mathrm{Pr}^{\frac{1}{3}},\ \mathrm{Pr} = \frac{c_p\mu_g}{\kappa_g}. \tag{11}$$

Here μ_g and κ_g represent the viscosity and thermal conductivity of the gas, respectively.

To define a multiphase flow, four non-dimensional parameters are required. For the gas phase, we have selected Knudsen and Mach numbers which together can measure the thermal non-equilibrium level. For the solid phase, the following two parameters are used: Particulate loading, which is defined as the density ratio of the two phases and can be a representative of the drug dose in the case of needle-free devices; Stokes number, which is an indicator of the level of coupling between phases. In a one-way coupled algorithm (where the gas phase is not affected by the solid phase), the source terms are absent.

III. SECOND-ORDER BOLTZMANN-CURTISS-BASED HYDRODYNAMICS MODEL FOR MODELING GAS IN THERMAL NON-EQUILIBRIUM USING THE METHOD OF MOMENTS

A. Conservation laws from the Boltzmann-Curtiss kinetic equation

Because of the collisional invariant properties of mass, momentum, and energy, the exact conservation laws can be derived from the Boltzmann-Curtiss kinetic transport equation. The Boltzmann-Curtiss kinetic equation for diatomic (and linear polyatomic) molecules with a moment of inertia I_m and an angular momentum **j** can be expressed as follows,[57]

$$\left(\frac{\partial}{\partial t} + \mathbf{v}\cdot\nabla + \frac{j}{I_m}\frac{\partial}{\partial \psi} + F\cdot\nabla_v\right) f\left(\mathbf{v},\mathbf{r},\mathbf{j},\psi,t\right) = C[f], \tag{12}$$

where $f, \mathbf{v}, \mathbf{r}, \psi, j$ and $C[f]$ represent the distribution function, the particle velocity, the particle position, the azimuthal angle associated with the orientation of the particle, the magnitude of the angular momentum vector **j**, and the collision integral, respectively. F is the external force on the unit mass and ∇_v denotes the gradient vector in the velocity space. The Boltzmann-Curtiss kinetic equation describes the changes in the probability distribution

function along a molecular pathway due to intermolecular collisions and under the presence of external force *F*.

After differentiating the statistical definition of the conserved variables with time and combining them with the Boltzmann-Curtiss kinetic equation, the following conservation laws, all of which are an exact consequence of the Boltzmann-Curtiss kinetic equation, can be derived:[40, 58, 59]

In the absence of external force,

$$\frac{\partial}{\partial t}\begin{bmatrix}\rho\\ \rho\mathbf{u}\\ \rho E\end{bmatrix}+\nabla\cdot\begin{bmatrix}\rho\mathbf{u}\\ \rho\mathbf{u}\mathbf{u}+p\mathbf{I}\\ \left(\rho E+p\right)\mathbf{u}\end{bmatrix}+\nabla\cdot\begin{bmatrix}0\\ \boldsymbol{\Pi}+\Delta\mathbf{I}\\ \left(\boldsymbol{\Pi}+\Delta\mathbf{I}\right)\cdot\mathbf{u}+\mathbf{Q}\end{bmatrix}=0. \tag{13}$$

There are two different sets of macroscopic variables; the conserved variables (ρ, $\rho\mathbf{u}$, and ρE) and the non-conserved variables ($\boldsymbol{\Pi}$, Δ, and $\mathbf{Q}$), where $\mathbf{u}$ is the bulk velocity vector, E is the total energy density, while $\boldsymbol{\Pi}$, Δ, and $\mathbf{Q}$ representing the shear stress tensor, the excess normal stress, and the heat flux, respectively. It is essential to emphasize that the set of equations (13) remains open until the exact relations of non-conserved variables are determined. Because of the presence of non-conserved variables (whose molecular definitions do not yield a collisional invariant), the evolution equations of these variables should be derived.

B. Boltzmann-Curtiss-based constitutive relationships for the gas phase

The same approach used to derive the conservation laws can be applied to the derivation of the evolution equation of non-conserved variables. After differentiating the statistical definition of the corresponding non-conserved variables with time and combining them with the Boltzmann-Curtiss kinetic equation, the following first-order Boltzmann-Curtiss-based constitutive model of the shear stress tensor, the excess normal stress, and heat flux vector can be derived:

$$\begin{aligned}\boldsymbol{\Pi}_g &= -2\mu_g\left[\nabla\mathbf{u}_g\right]^{(2)},\\ \Delta_g &= -\mu_b\nabla\cdot\mathbf{u}_g,\\ \mathbf{Q}_g &= -\kappa_g\nabla T_g.\end{aligned} \tag{14}$$

The symbol $[\mathbf{A}]^{(2)}$ denotes the traceless symmetric part of the second-rank tensor **A**. It should be mentioned that these first-order linear relations were obtained after very crude first-order approximations; all kinematic terms except for the thermodynamic force term were neglected in the evolution equations, and the collision-related dissipation terms were linearized. Moreover, a distinction should be made regarding Navier-Fourier (NF) and Navier-Stokes-Fourier (NSF) relations. In the latter, Stokes' hypothesis, $\mu_b = 0$, was applied.

Similarly, the second-order Boltzmann-Curtiss-based constitutive models can be derived by first differentiating the statistical definition of the non-conserved variables with time and then combining them with the Boltzmann-Curtiss kinetic equation. Once the two tenets—Eu's cumulant expansion based on the canonical distribution function in the exponential form to the explicit calculation of the dissipation term,[43, 44] and Myong's closing-last balanced closure[59]—are applied to the evolution equations and after introducing the so-called adiabatic approximation (derived from the observation that the relaxation times of the non-conserved variables are very short, being on the order of 10^{-10} second), the following second-order constitutive model can be derived from the Boltzmann-Curtiss kinetic equation:[40, 58, 59]

$$
\begin{aligned}
&\hat{\mathbf{\Pi}} q_{2nd}\left(c\hat{R}\right) = \left(1+ f_b\hat{\Delta}\right)\hat{\mathbf{\Pi}}_0 + \left[\hat{\mathbf{\Pi}}\cdot\nabla\hat{\mathbf{u}}\right]^{(2)},\\
&\hat{\Delta} q_{2nd}\left(c\hat{R}\right) = \hat{\Delta}_0 + \frac{3}{2}\left(\hat{\mathbf{\Pi}} + f_b\hat{\Delta}\mathbf{I}\right):\nabla\hat{\mathbf{u}},\\
&\hat{\mathbf{Q}} q_{2nd}\left(c\hat{R}\right) = \left(1+ f_b\hat{\Delta}\right)\hat{\mathbf{Q}}_0 + \hat{\mathbf{\Pi}}\cdot\hat{\mathbf{Q}}_0,\\
&\text{where } q_{2nd}\left(c\hat{R}\right) = \frac{\sinh(c\hat{R})}{c\hat{R}},\quad \hat{R}^2 \equiv \hat{\mathbf{\Pi}}:\hat{\mathbf{\Pi}} + (5-3\gamma) f_b\hat{\Delta}^2 + \hat{\mathbf{Q}}\cdot\hat{\mathbf{Q}}.
\end{aligned}
\tag{15}
$$

The caret (ˆ) over a symbol represents a quantity with the dimension of stress to pressure. The values of $\mathbf{\Pi}_0$, Δ_0, and $\mathbf{Q}_0$ are determined by the Newtonian law of shear and bulk viscosity and the Fourier law of heat conduction, respectively. $\hat{R}$ represents the Rayleigh-Onsager dissipation function,[60] and the constant c has a value between 1.0138 (Maxwellian) and 1.2232; for instance, 1.018 for the nitrogen gas molecule.[40, 58, 59] The Rayleigh-Onsager dissipation function gives a direct measure of departure from thermal equilibrium. The first-order cumulant approximation for the nonlinear factor '$q_{2nd}\left(c\hat{R}\right)$' in Eq. (15) describes the mode of energy dissipation accompanying the irreversible processes and is directly related to the nonequilibrium entropy production in the system. The factor $f_b = \mu_b/\mu$ is the ratio of the bulk

viscosity to the shear viscosity. Its value may be experimentally determined using a sound wave absorption measurement; for instance, 0.8 for the nitrogen gas molecule and almost 1000 for carbon dioxide.

The closing-last balanced closure[59] applied to derive Eq. (15) is based on a keen observation of the essence of the closure problem in a complex system: when closing open terms, the number of places to be closed is two (movement and collision), rather than one (movement only) and thus the order of approximations in handling the two terms must be the same to satisfy balancing. The present balanced closure effectively resolves the weakness of Eu's original closure,[44] which was strongly criticized for its inconsistency.

Unlike the original Boltzmann kinetic equation, the Boltzmann-Curtiss kinetic equation additionally introduces the angular momentum and azimuth angle associated with the rotational mode of molecules. In the present framework, the bulk viscosity of diatomic and polyatomic gases was viewed as a quantity directly related to the relaxation time associated with the rotational degrees of freedom. It was shown by McCourt *et al.*[61] (1990, p. 276) that the excess normal stress, Δ, appearing in the conservation law of momentum Eq. (13) is equivalent to the difference between the translational and rotational temperatures. Thus, the hydrodynamic equation can be formulated in two ways: either introducing the excess normal stress, Δ, and retaining the one temperature ($T_{trans\text{-}rot}$) concept or introducing two temperatures (T_{trans} & T_{rot}) but assuming no excess normal stress. The former was employed in the present study because not only is it a natural extension of the Navier-Fourier constitutive laws, but it connects more naturally with the laws of thermodynamics.

To simulate the second-order effects of diatomic and polyatomic gases with activated vibrational degrees of freedom and vibrational-transrotational non-equilibrium, Mankodi and Myong[46] developed a new set of hydrodynamic equations based on the two-temperature ($T_{trans\text{-}rot}$ & T_{vib}) formulation. However, the vibrational non-equilibrium effect can be ignored in the present study because the temperature range is much lower than the onset temperature for vibrational excitation (800-1000 K).

It was noted in the past that Eu's canonical distribution function in the exponential form may have some difficulty when it is truncated to a finite number of terms. A numerical difficulty may arise when calculating the normalization factor associated with the canonical distribution function because the heat flux contribution containing the 3rd-order term for the integrand may give rise to the divergence-causing problem. Eu showed, however, that this difficulty can be

avoided if the set is truncated in such a way as to produce a truncated distribution function in the 4th-order for the integrand while ensuring convergence of the integral.[62]

Even though the second-order constitutive model in Eq. (15) involves highly nonlinear implicit algebraic equations, they can be easily solved numerically for the given thermodynamic driving forces, based on the concept of decomposition and the method of iteration.[40, 58, 59]

Once the second-order constitutive model in Eq. (15) is derived, it can be straightforwardly integrated through $\mathbf{\Pi}_g$ and $\mathbf{Q}_g$ terms with the conservation laws (Eqs. (1) and (2)) governing the gas phase within the two-fluid model. This integration process is similar to how other constitutive relations are combined with the conservation laws in the two-fluid model or a standalone single-phase case.

IV. NUMERICAL MODELING, VERIFICATION, AND VALIDATION

A. Numerical methodology

The mathematical model described in Sections II and III is discretized using a finite volume method. An explicit time integration method (a low-storage fourth-order Runge-Kutta scheme) is applied to solve the semi-discrete equations. The hybrid HLLC-AUSM method of Koop[63] is used as the numerical flux function. The method can be used for both the gas and solid phases. In the AUSM flux and its variant, the inviscid flux is divided into convection and a pressure flux, and hence it may be useful for a pressureless system of equations. The principal idea in the AUSM scheme is to decompose the numerical flux into a convective and a pressure vector as follows:

$$\mathbf{F(U)} \cdot \hat{\mathbf{n}} = \dot{m}\mathbf{F}_{\text{convective}} + \mathbf{F}_{\text{pressure}}, \tag{16}$$

where $\mathbf{F}_{\text{convective}}$ and $\mathbf{F}_{\text{pressure}}$ are defined as

$$\mathbf{F}_{\text{convective}} = \begin{bmatrix} 1 \\ \mathbf{U}_{L,R} \\ H_{L,R} \end{bmatrix}, \quad \mathbf{F}_{\text{pressure}} = \begin{bmatrix} 0 \\ \bar{p}\hat{\mathbf{n}} \\ 0 \end{bmatrix}. \tag{17}$$

Here $\hat{\mathbf{n}}$ is the unit normal vector of the face, and $\dot{m}$ is the HLLC mass flux given by

$$\dot{m}=\begin{cases}\rho_L u_L & 0\le S_L\\ \rho_L u_L+S_L(\rho_L\dfrac{S_L-u_L}{S_L-S_*}-\rho_L) & S_L<0\le S_*\\ \rho_R u_R+S_R(\rho_R\dfrac{S_R-u_R}{S_R-S_*}-\rho_R) & S_*<0\le S_R\\ \rho_R u_R & S_R<0\end{cases} \tag{18}$$

The wave speeds S are given by

$$\begin{aligned}&S_L=\min\{u_L-a_L,u_R-a_R\},\\ &S_R=\max\{u_L+a_L,u_R+a_R\},\\ &S_*=\frac{p_R-p_L+\rho_L u_L(S_L-u_L)-\rho_R u_R(S_R-u_R)}{\rho_L(S_L-u_L)-\rho_R(S_R-u_R)}.\end{aligned} \tag{19}$$

In the above relations, a_L and a_R are the left and right speeds of sound.

The pressure $\bar{p}$ in the pressure part of the flux of Eq. (17) is given by a fifth-order polynomial:

$$\begin{aligned}&\bar{p}=\mathcal{P}^{+}_{(5)}(M_L)\,p_L+\mathcal{P}^{-}_{(5)}(M_R)\,p_R\\ &-K_u\mathcal{P}^{+}_{(5)}(M_L)\mathcal{P}^{-}_{(5)}(M_R)(\rho_L+\rho_R)(u_R-u_L)\,f_c\,\frac{a_L+a_R}{2}.\end{aligned} \tag{20}$$

The pressure functions in the above polynomial are defined as

$$\mathcal{P}^{\pm}_{(5)}=\begin{cases}(1/M)\,\mathcal{M}^{\pm}_{(1)} & |M|\ge 1\\ \mathcal{M}^{\pm}_{(2)}\left[(\pm 2-M)\mp 16\gamma M\,\mathcal{M}^{\mp}_{(2)}\right] & |M|<1\end{cases} \tag{21}$$

in which split Mach functions are given by

$$\begin{aligned}&\mathcal{M}^{\pm}_{(1)}=\frac{1}{2}\left(M\pm|M|\right),\\ &\mathcal{M}^{\pm}_{(2)}=\pm\frac{1}{4}\left(M\pm 1\right)^2.\end{aligned} \tag{22}$$

The definition of the remaining variables is as follows

$$
\begin{aligned}
&f_c = M_0\left(2 - M_0\right),\\
&M_0 = \min\left(1, \max\left(\bar{M}^2, M_\infty^2\right)\right),\\
&\bar{M}^2 = \frac{u_L^2 + u_R^2}{2\left(\frac{a_L + a_L}{2}\right)^2},\\
&\gamma = \frac{3}{16}\left(-4 + 5 f_c^2\right), \quad 0 \le K_u \le 1.
\end{aligned}
\tag{23}
$$

B. Treatment of the non-strictly hyperbolic equations of solid phase

In this study, a simple yet effective strategy is applied as a relaxation method. The idea was inspired by a strategy initially developed in computational magnetohydrodynamics (MHD)[64-66] and has been applied in other fields, including aircraft icing in the atmosphere.[67] The approach is tested for the two-fluid equation model of dusty gases in a modal discontinuous Galerkin and finite volume frameworks.[27, 31] The basic idea is to add and subtract a pressure-related term to the momentum and energy equations of the dust phase. Even though this manipulation does not have any algebraic consequences, from a numerical point of view, the new system has an obvious advantage, recovering the strict hyperbolicity of the equation. The equation of the dust phase (in the Euler-Euler model) after the addition and subtraction of a pressure-related term can be written as follows,

$$
\partial_t \begin{bmatrix} \alpha_s\rho_s \\ \alpha_s\rho_s\mathbf{u}_s \\ \alpha_s\rho_s E_s \end{bmatrix} + \nabla\cdot \begin{bmatrix} \alpha_s\rho_s\mathbf{u}_s \\ \alpha_s\rho_s\mathbf{u}_s\mathbf{u}_s + p_s\mathbf{I} - p_s\mathbf{I} \\ (\alpha_s\rho_s E_s + p_s - p_s)\mathbf{u}_s \end{bmatrix} = -\mathbf{S}\,. \tag{24}
$$

Equivalently in split form,

$$
\partial_t \begin{bmatrix} \alpha_s\rho_s \\ \alpha_s\rho_s\mathbf{u}_s \\ \alpha_s\rho_s E_s \end{bmatrix} + \nabla\cdot \begin{bmatrix} \alpha_s\rho_s\mathbf{u}_s \\ \alpha_s\rho_s\mathbf{u}_s\mathbf{u}_s + p_s\mathbf{I} \\ (\alpha_s\rho_s E_s + p_s)\mathbf{u}_s \end{bmatrix} = \nabla\cdot \begin{bmatrix} 0 \\ p_s\mathbf{I} \\ p_s\mathbf{u}_s \end{bmatrix} - \mathbf{S} \tag{25}
$$

In this equation, the inviscid flux is equivalent to that of the Euler equation of the gas phase. Thus, the conservation law can be considered strictly hyperbolic, and the additional term on the right-hand side can be handled in a way similar to the way source terms are treated.

C. Verification of the implementation of the NCCR

The second-order Boltzmann-based model, also known as nonlinear coupled constitutive relationships (NCCR), has been validated in a variety of frameworks by the authors[39, 45, 46, 68] as well as other groups.[69-72] In this section, we verify the implementation of the model in the newly developed solver for the low-speed micro-Poiseuille and high-speed shock tube problems.

1. Micro-Poiseuille flow (pressure-driven flow inside a microchannel)

The two-dimensional steady-state Poiseuille flow of compressible argon gas through microchannels was considered. The laminar flow is induced by the pressure difference (the inlet and outlet pressures, P_{in} and P_{out}) imposed on a channel with length L and height H. The walls of the channel are kept at the same constant temperature of T_w which is equal to the upstream flow temperature T_{in}. The flow velocity generated by the pressure difference varies in both the x and y directions. A schematic of the flow is shown in Fig. 2.

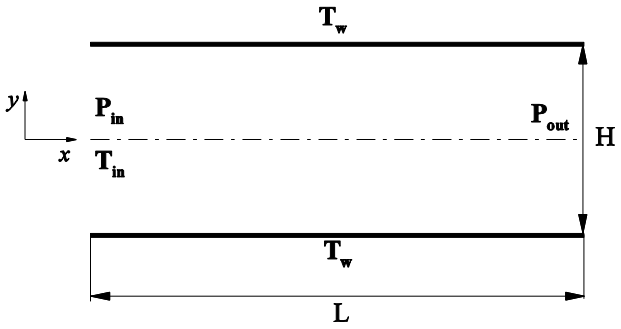

Fig. 2. Schematic drawing of the flow geometry.

Here, a microchannel with a height of 1 μm and a length of 8 μm is considered. The wall temperature and inlet gas temperature are set to 300 K. The inlet pressure is set to 1.2 atm and a pressure ratio of 2.4 is applied. This setup will lead to Knudsen numbers varying from 0.044 to 0.11 alongside the channel. The simulations were conducted for monatomic (argon) gas, the thermophysical properties of which are summarized in Table I.

Table I. Thermophysical properties of the gases used in simulations of micro-Poiseuille flow.

Gas	Diameter ($\times 10^{10}$ m)	Molecular mass ($\times 10^{27}$ kg)	Specific gas constant, R (J/kg·K)	Reference viscosity, μ_{ref} ($\times 10^{-5}$ Pa·s)	Specific heat ratio, γ	Viscosity ratio, f_b
Argon (Ar)	4.17	66.3	208	2.125	5/3	0

Maxwell velocity slip and Smoluchowski temperature jump boundary conditions[73-76] are applied in the present study:

$$\mathbf{u} = \mathbf{u}_W - \left(\frac{2-\sigma_u}{\sigma_u}\right)\frac{\lambda}{\mu}\mathbf{\Pi}_{Tangential} - \frac{3}{4}\frac{\Pr(\gamma-1)}{\gamma p}\mathbf{Q}_{Tangential}, \tag{26}$$

$$T = T_W - \left(\frac{2-\sigma_T}{\sigma_T}\right)\frac{2\gamma}{(\gamma+1)}\frac{\lambda}{\Pr\kappa}\mathrm{Q}_{Normal}, \tag{27}$$

where σ_u and σ_T are momentum and thermal accommodation coefficients, respectively, and the subscript W stands for quantities at the wall. The implementation of the boundary conditions is verified in the problem of micro-Poiseuille flow, by comparing the results with the DSMC solutions of the in-house code previously validated in several studies by the authors.[77-80] As shown in Fig. 3, with the application of slip boundary conditions, the solutions would be much closer to the DSMC. It can also be observed that the second-order Boltzmann-based model (NCCR) provides solutions that are in very good agreement with the DSMC solution even in the downstream section of the microchannel, where rarefaction effects are more dominant.

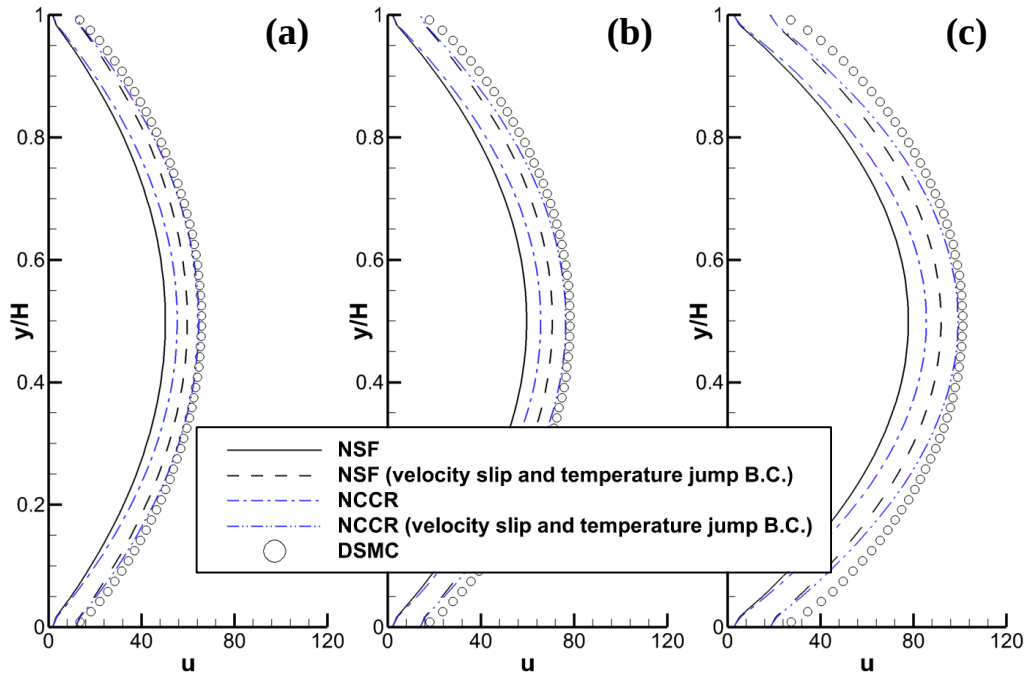

Fig. 3. Comparison of the velocity solution in different sections of a microchannel with DSMC solutions: (a) 0.2*L*; (b) 0.5*L*; (c) 0.8*L*.

2. Multidimensional flows inside the micro shock tube

To verify the pure gas simulation of the micro shock tube, the case investigated by Zeitoun *et al.*[22] was analyzed. Schematics of the two-dimensional microchannel and three-dimensional microtube, employing boundary conditions, domain size, and a sample grid, are depicted in Fig. 4. Following Zeitoun *et al.*[22], the gaseous flow of argon in a plane channel with a height and length of $2H$ = 5 mm and $L = 32H$ was simulated. The driver and driven gas pressures are set equal to 525.98 Pa and 44.2 Pa, which corresponds to a theoretical shock Mach (M_s) number of 1.6. For this case, the Knudsen number, i.e., the ratio of the mean free path to the channel height (λ/H) based on the driver gas properties, is equal to 0.05. A grid almost identical to the one used by Zeitoun *et al.*[22] is applied for the two-dimensional case. For the tube case (three-dimensional) because of the problem symmetry, a quarter of the domain is simulated. The domain is discretized in such a way that the characteristic grid size is identical to the two-dimensional case.

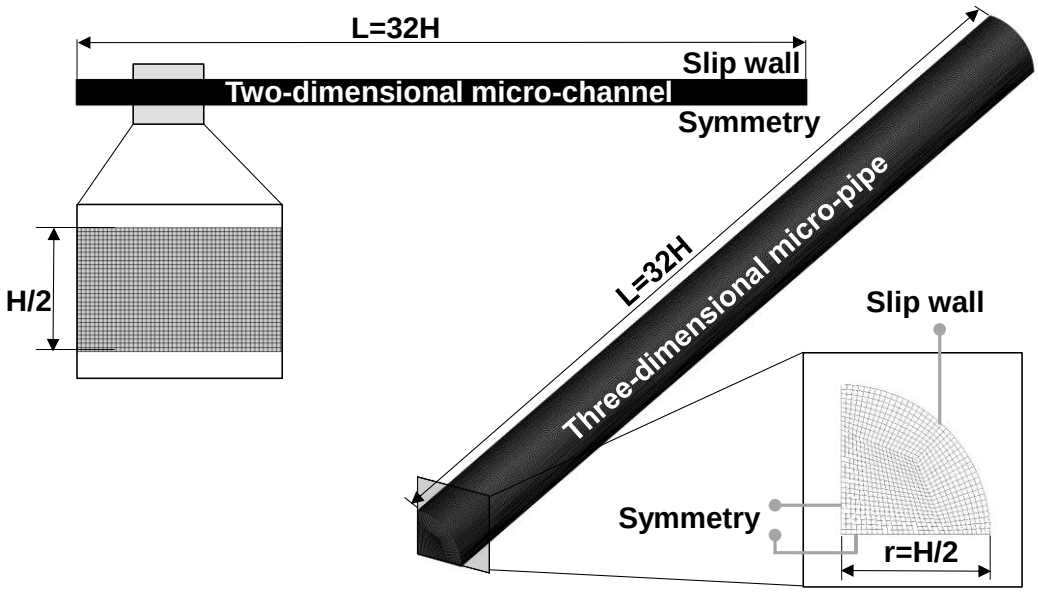

Fig. 4. A schematic of the two-dimensional microchannel and three-dimensional micro-tube, applied boundary conditions, computational grid, and domain size.

The temperature solutions achieved by the second-order Boltzmann-based constitutive relationships, compared with the BGKS, DSMC, and NSF solutions of Zeitoun *et al.*[22] are shown in Fig. 5. Again, good agreement is observed. The only model that slightly underpredicts the location of the shock front is the NSF without the application of slip and jump boundary conditions.

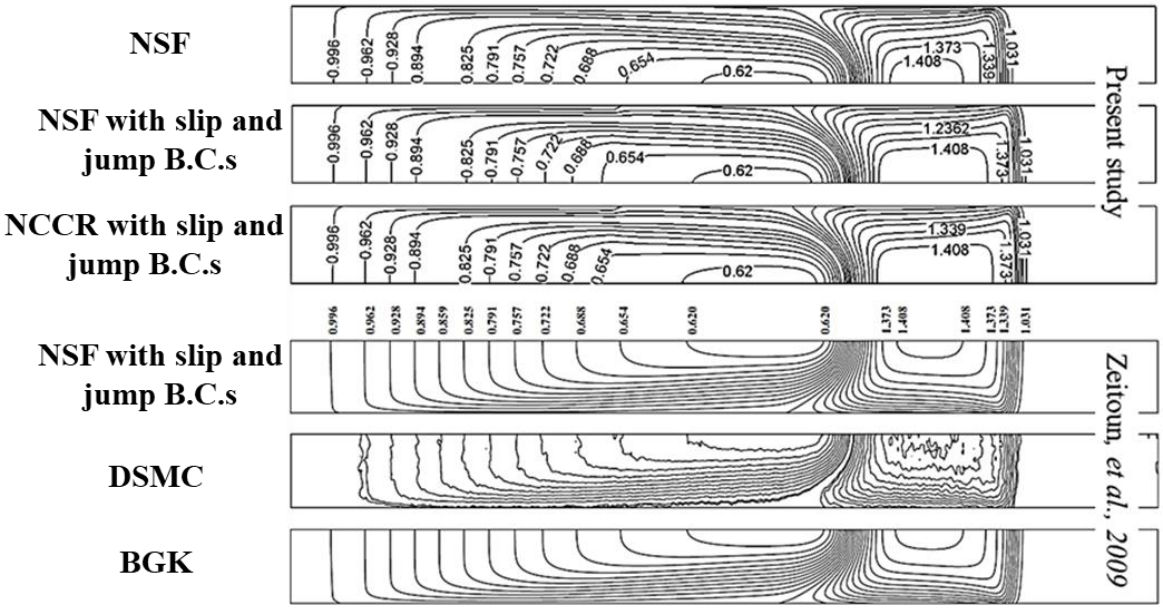

Fig. 5. Comparison of temperature solution with continuum-based and DSMC solutions of Zeitoun *et al.*[22] (M_s = 1.6, Kn = 0.05).

The wave diagram of the contact and shock wave motion in the center of the channel is plotted in Fig. 6. For the case of Kn = 0.05, there is a slight difference in the prediction of the location of the contact and shock wave when slip and jump boundary conditions are applied. The NSF and NCCR models show almost no deviation. For the case of Kn = 0.5, however, the models show slightly different predictions. For this case the deviation of the models when slip and jump boundary conditions are applied is considerable. Moreover, it can be seen that the shock wave does not travel at a constant speed as the Knudsen number increases. Such an analysis was also conducted for the one-dimensional cases of pure gas and dusty gas and will be discussed in Section V.A.

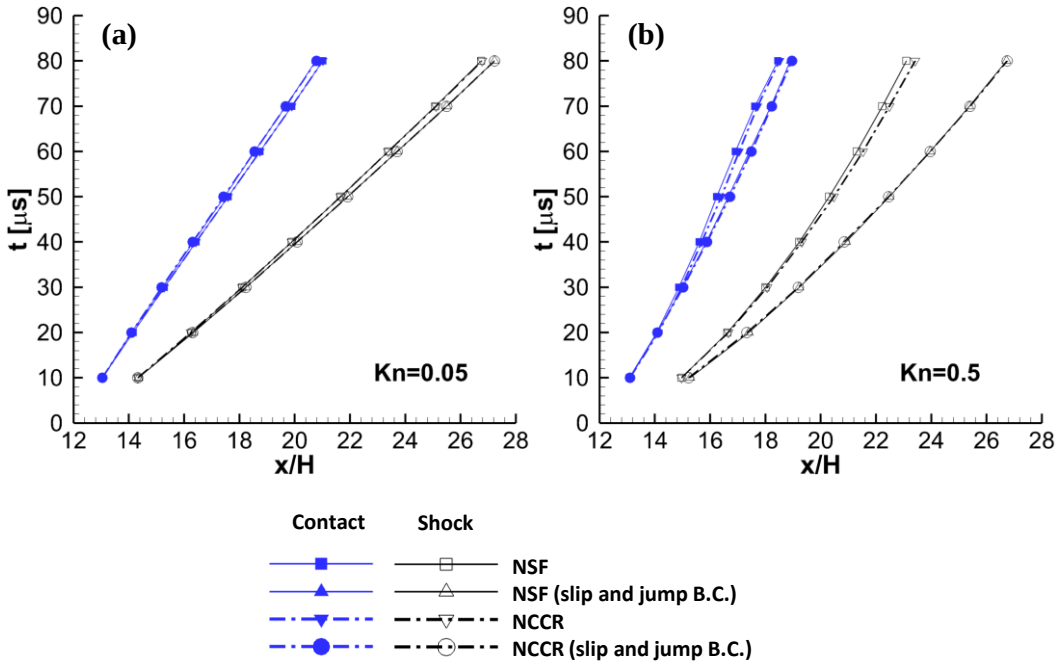

Fig. 6. Wave diagram of the shock wave and contact surface for two different Knudsen numbers (blue: contact discontinuity and black: shock waves): (a) Kn=0.05; (b) Kn=0.5.

V. RESULTS AND DISCUSSIONS

A. One-dimensional Sod shock-tube problem

Based on the shock-tube theory, after the rupture of a diaphragm separating inviscid gases with a constant γ and different pressures, a shock wave is generated and moves to the low-pressure side at a constant speed, $\mathbf{u}_s$. This wave is followed by the contact discontinuity moving with a constant speed, $\mathbf{u}_c = \mathbf{u}_2 = \mathbf{u}_3$. Further, an expansion fan travels to the opposite side of the channel, as shown in Fig. 7.

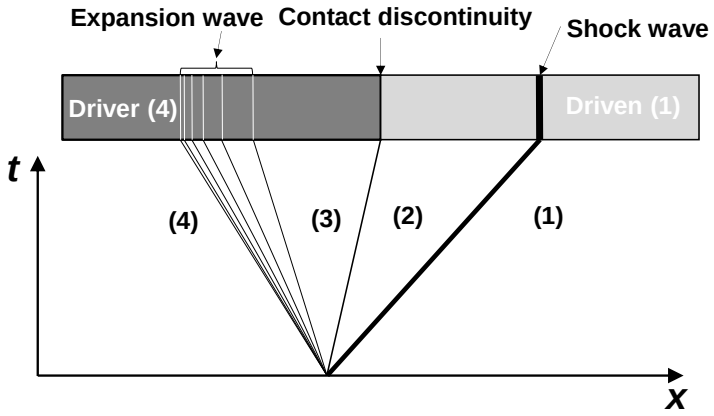

Fig. 7. The schematic of a shock tube and numbering of domains separated by waves.

The classical Sod shock tube problem will be investigated in detail to check the rarefaction effects as well as the effects of the addition of particles to the domain, as the flow becomes rarefied. Such one-dimensional flow properties, free from the geometrical and boundary condition complexities, are a suitable representative of the flow types of interest in this study. In the current study, this problem was investigated in detail to provide a deeper understanding of governing physics. A shock tube with a test section length of L = 10 m, a pressure ratio of 10, air as the working gas (specific heat ratio of γ = 1.4 and a gas constant of R = 287 J/Kg·K), and a uniform temperature of 300K was simulated. The diaphragm is located at x/L = 0.4. The pressures of both the driver and driven sections were varied to obtain different rarefaction levels (Knudsen number variation).

1. Rarefaction effects on the transient flow inside the shock tube

Next are investigated the rarefaction effects in the Sod shock-tube problem. Inviscid solutions are compared with viscous solutions of both the first-order (NSF) and second-order (NCCR) Boltzmann-based constitutive equations as shown in Fig. 8. Knudsen number is defined as the ratio of the mean free path in the driver section to channel height. As expected, all the models converge to a unique solution for low Knudsen number set-ups (Kn = 0.0053). When the Knudsen number is increased to 0.053 (i.e., below the slip regime limit), the NSF and NCCR models slightly deviate from the inviscid theory explained by Euler equations. As the Kn increases further, the viscous model solutions diverge from the inviscid theory; however, both NSF and NCCR are in good agreement, even for Kn = 0.53 which is well above the slip regime. For larger Kn numbers (in the transition regime), the NSF and NCCR theories seem to deviate more from each other when considering the percentage of absolute deviation.

An interesting feature of high Knudsen number flow is the placement of the rarefaction tail, contact discontinuity, and the fully dispersed shock wave at the same place. In fact, in such high Knudsen flows (for the investigated pressure ratio), no shock wave is formed. It is crucial to highlight that even for lower Knudsen numbers, as the parameter variations are not abrupt, the application of the term "shock wave" may be misleading. However, we use the term to refer to the condition when a variation in density, pressure, temperature, and velocity is recognizable, even though it may be slow and smooth. To plot wave diagrams, the first drop in the temperature profile (from left to right) is detected as the rarefaction head, the first location where the maximum temperature is reached is marked as the contact, and the first increase in temperature moving from right to left is marked as the shock location.

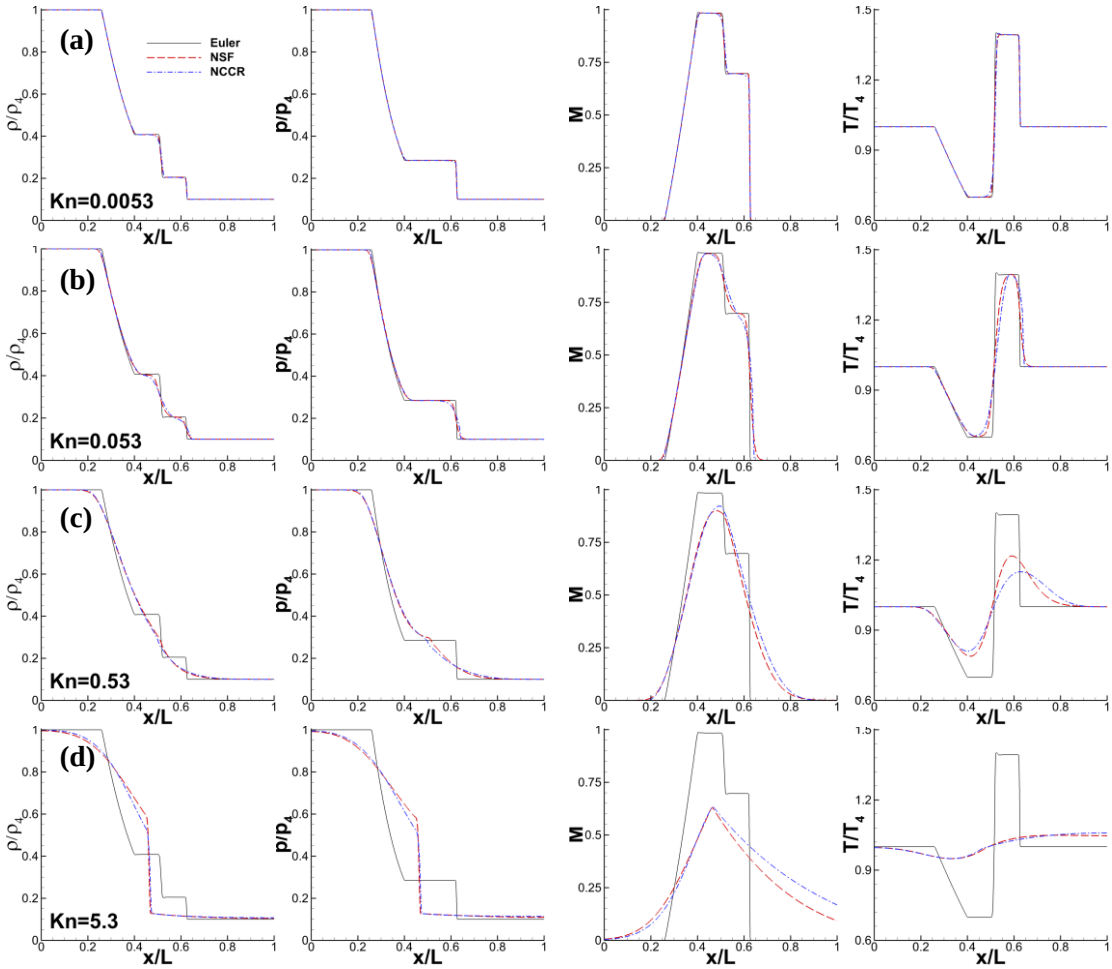

Fig. 8. Rarefaction effects in one-dimensional Sod shock-tube (Euler-NSF-NCCR): (a) Kn=0.0053; (b) Kn=0.053; (c) Kn=0.53; (d) Kn=5.3.

The wave diagrams for the shock, contact discontinuity, and rarefaction waves are provided in Fig. 9 to demonstrate how rarefaction affects the dynamics of the flow. As the

figure demonstrates, all the waves and discontinuities are accelerated when the Knudsen number increases. Furthermore, the hot flow length (the distance between the shock and the contact) increases as the flow rarefies. For high Knudsen cases, the temperature increase in the hot flow region is much lower than in low Knudsen cases.

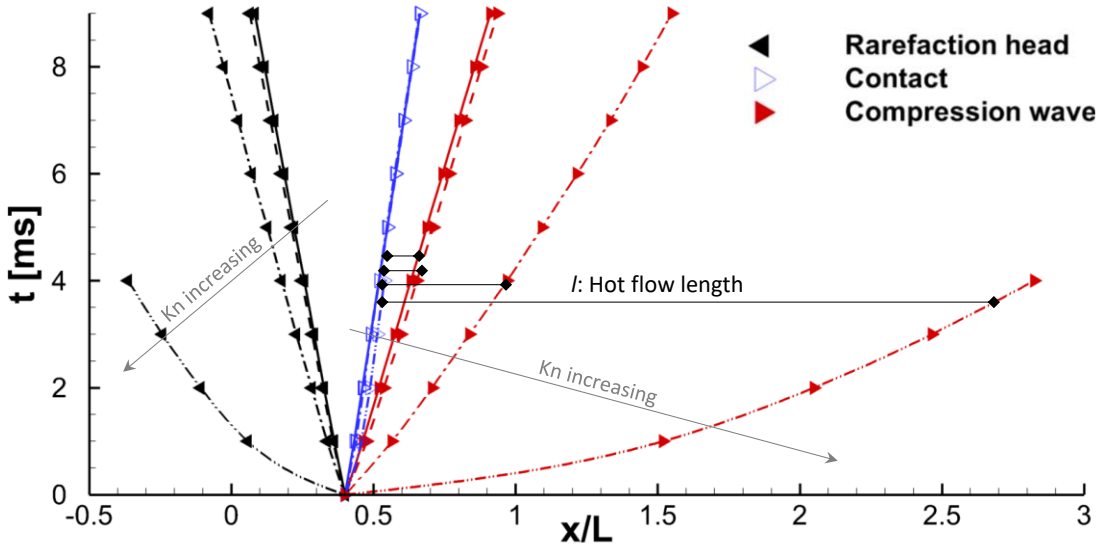

Fig. 9. Rarefaction effects on the motion of the waves (x-t diagram): Kn=0.0053 (solid), Kn=0.053 (dashed), Kn=0.53 (dash-dot), Kn=5.3 (dash-dot-dot).

2. Bulk viscosity effects on the structure of the discontinuities in the Sod shock tube problem

In the case of diatomic and polyatomic gases with an internal degree of freedom, there is a property called bulk viscosity. Bulk viscosity is a material property relevant to characterizing fluid flow. This property typically causes viscous damping brought on by volumetric straining. This viscosity appears in connection with the compression or dilatation, the inner structure of strong shock waves, the decay rate of turbulent kinetic energy, and sound wave absorption of the gas.[39, 43-46, 61, 81, 82] As indicated in Eqs. (14) and (15), the bulk viscosity contributes directly to the excess normal stress, Δ. The present second-order constitutive model has been validated through experiments and DSMC on the inner structure of shock waves in diatomic and polyatomic gases in previous studies (Fig. 4 of Myong[39], Figs. 17-19 of Mankodi and Myong[46], Fig. 11 of Singh *et al.*[75], and Figs. 14 and 15 of Singh *et al.*[81]).

As explained by McCourt *et al.*[61] in 1990, the hydrodynamic equation can be formulated either by introducing the excess normal stress, Δ, and retaining the one temperature ($T_{trans\text{-}rot}$) concept or by introducing two temperatures (T_{trans} & T_{rot}) but assuming no excess normal stress.

Recently, models that incorporate rotational energy relaxation, along with a variable viscosity ratio linked to local temperature, have also been introduced.[83] We employ the former formulation in the present study. To investigate the role of bulk viscosity in the evolution of the flow in the Sod shock tube problem, pseudo gases with various values of viscosity ratios f_b, were simulated.

Fig. 10 shows how the variation of this parameter can affect the structure of the gaseous flow in the shock tube problem. In this figure, normalized values of density, pressure, temperature, Mach number, Rayleigh-Onsager dissipation number, and excess normal stress are compared for various values of f_b. This comparison was conducted for two different Knudsen numbers. Fig. 10(a) represents the case with a Knudsen number of 0.0053. As can be observed in the figure, an increase in the viscosity ratio can significantly affect the structure of all discontinuities in the problem. Interestingly, the variations are not monotone and changes in trends for different features were observed. For example, the rarefaction wave initially intensified as the bulk viscosity was increased, however, for f_b values higher than 20, the expansion wave was attenuated as demonstrated, in the density, pressure, and temperature profiles. It was also observed that the maximum value of the Mach number initially increased. However, with a further increase in the f_b number this value dropped. Finally, it can be noted that the general trend regarding the effects of f_b and Kn values observed in Fig. 10 is consistent with the results inferred from Eq. (15) of the Rayleigh-Onsager dissipation function, $\hat{R} \approx \mathrm{Kn} \cdot M[1+(5-3\gamma) f_b + \cdots]^{1/2}$, measuring the level of departure from thermal equilibrium.

The contact discontinuity is also affected by the variation of this parameter. For moderate f_b numbers, a relaxation zone is generated before the shock wave. This is equivalent to a double-layer structure: a steep change in properties followed by a thick relaxation zone to reach equilibrium downstream.[84] Similar effects have been observed in the stationary shock structure problem using an extended thermodynamics approach by Taniguchi *et al.*[85]. However, for larger values ($f_b > 20$), the shock wave is attenuated, such that only a relaxation zone is recognizable.

These results give rise to intriguing solution profiles, where the contact discontinuity is associated with both rarefaction and shock waves. These findings can be also observed as the Knudsen number increases, as shown in Fig. 10(b). It is noteworthy that all the observed trends correlate with an increase in the Knudsen number. For example, the transitions from a normal shock to a double-layer shock, and from a double-layer to only a relaxation region, were

observed to occur at much lower values of f_b as the Knudsen number was increased. It is worth mentioning that an increase in the f_b number can lead to an increase in the shock wave thickness and speed of the shock front. This creates a numerical challenge, as a larger computational domain with a finer computational grid (especially in the case of double-layer shock) is required. Therefore, while the results in this work are presented for the range $0 < x/L < 1$, for larger f_b and Kn values larger domain sizes can be applied. The 0 to 1 range was merely selected to better represent the figures. A zoomed-out view of the solution is also shown in each plot in Fig. 10.

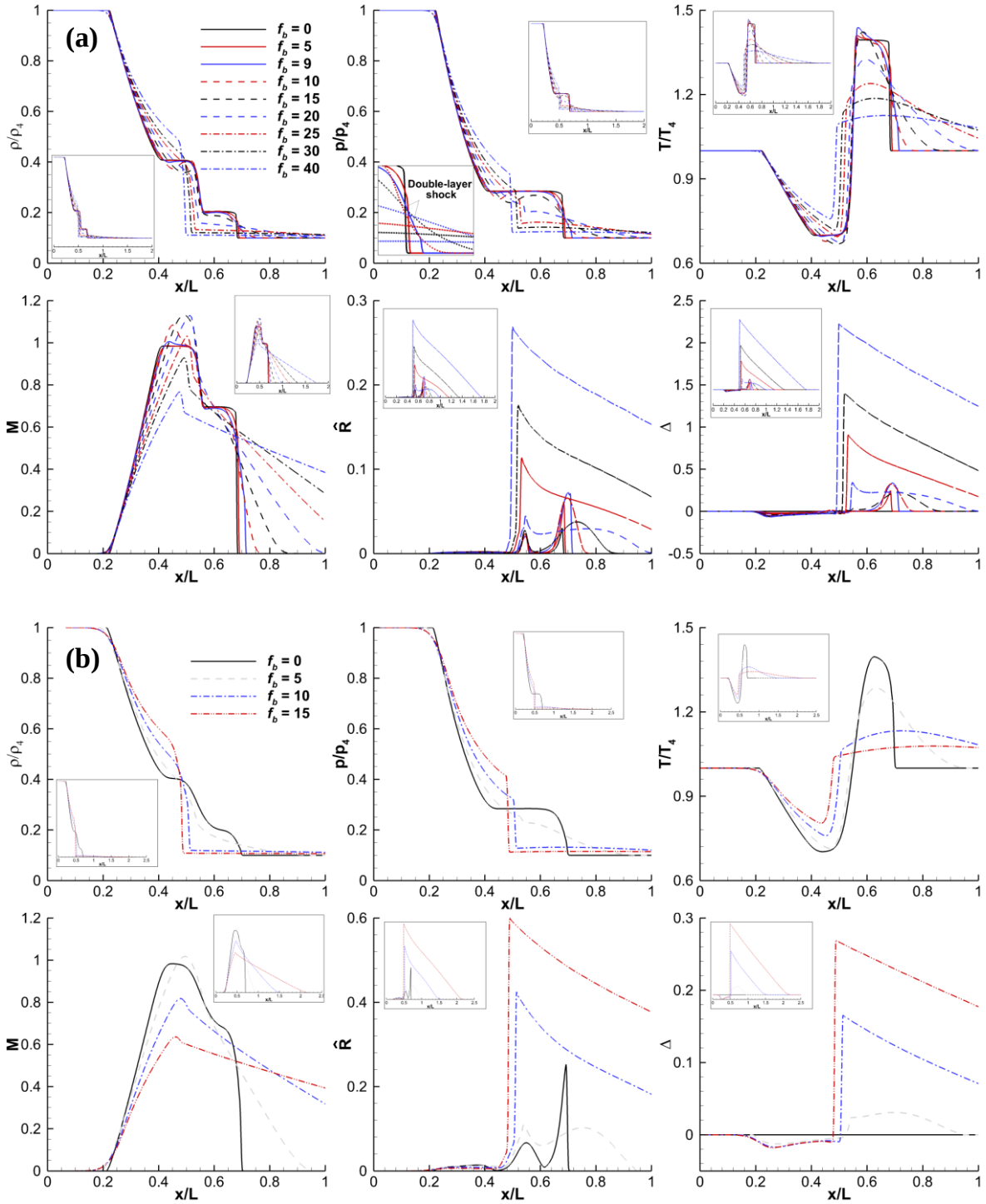

Fig. 10. Effects of bulk viscosity on the structure of the discontinuities at t = 3 ms: (a) Kn = 0.0053; (b) Kn = 0.053.

It is essential to recognize that such patterns can only be captured once a higher-order model is used. Comparing the solutions with the linear theory, even when the Stokes hypothesis is abandoned, confirms the aforementioned hypothesis. In Fig. 11, the time evolution of the flow

for two different Knudsen numbers and two gases with different bulk viscosity values is computed using both the linear (NF) and nonlinear (NCCR) theories.

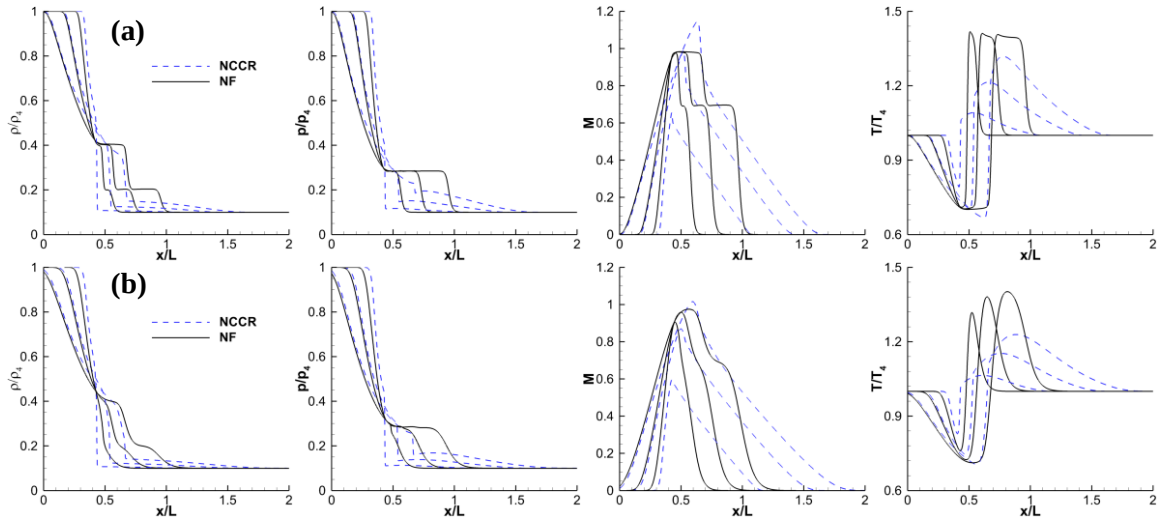

Fig. 11. Comparison of the linear theory (NF) with second-order theory (NCCR) for gases with large bulk viscosity values at different time steps: (a) Kn = 0.0053, f_b = 30; (b) Kn = 0.053, f_b = 10.

3. Effects of rarefaction on complex wave patterns inside a dusty gas shock tube

It should be emphasized that, unlike the single-phase flow in a shock tube, complex wave patterns (i.e., pseudo-compound waves as well as composite waves) may occur in problems where moving shocks interact with a dusty medium.[27] These patterns are shown in Fig. 12.

We are interested in investigating how rarefaction affects these complex patterns. For this purpose, a dusty shock tube problem is studied for three different particulate loadings and four Knudsen numbers, ranging from continuum to free-molecular regimes. The density and temperature solution of the gaseous phase in the multiphase setup is compared with the pure gas solution in Fig. 13. The complex wave patterns due to the presence of solid particles can be best recognized in the higher particulate loading case. It is apparent that with increasing Knudsen number, the reflected shock wave is strongly attenuated. Even for the case of Kn=0.053 and β=1.0, the reflected shock can hardly be distinguished. Also, the temperature variation is limited as dust particles are added. An interesting feature was observed in the case where both Knudsen and particulate loadings were large (Kn=0.53 and β=10.0).

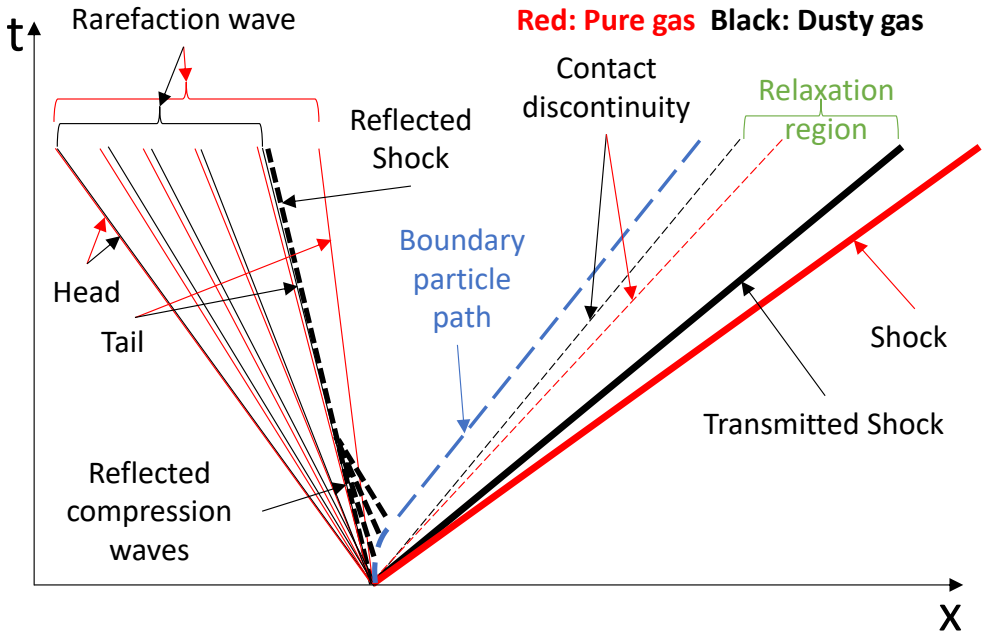

Fig. 12. Schematic of various wave structures in a 1-D dusty gas flow: The gas contact discontinuity and boundary particle path are initially located at the same position. Reproduced with permission from O. Ejtehadi, A. Rahimi, A. Karchani, R.S. Myong, "Complex wave patterns in dilute gas-particle flows based on a novel discontinuous Galerkin scheme," Int. J. Multiphase Flow 104, 125 (2018). Copyright 2018 Elsevier.

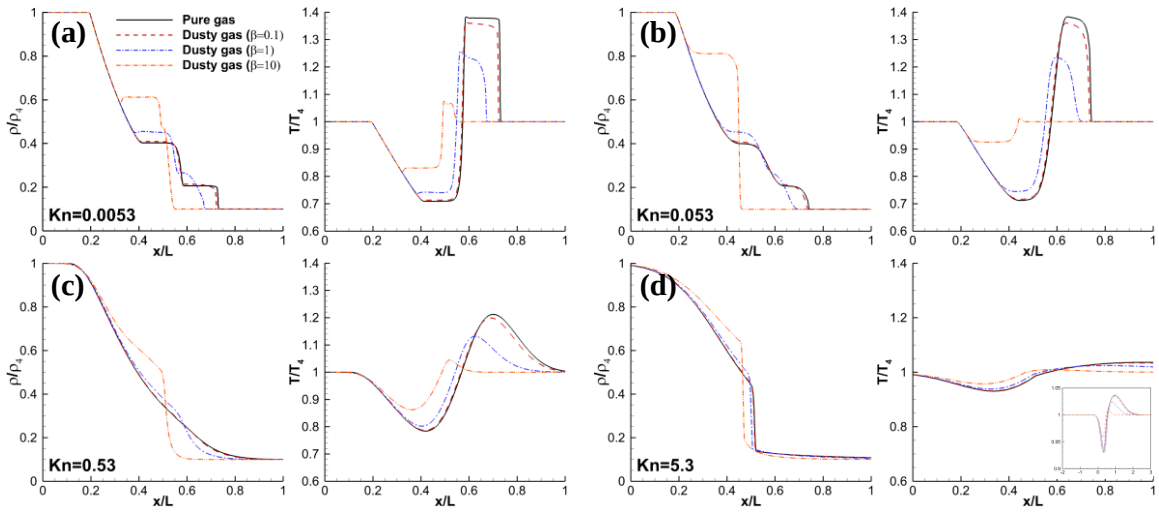

Fig. 13. Rarefaction effects on complex wave patterns (t = 0.006 s): (a) Kn=0.0053; (b) Kn=0.053; (c) Kn=0.53; (d) Kn=5.3.

Also shown in Fig. 14 are the wave diagrams of shock and expansion waves, as well as the contact discontinuity. As mentioned earlier, for highly rarefied flows, defining (or detecting) the shock wave based on the classical definition (sudden jump in properties) is not applicable

since the shock wave is highly smoothed. The rarefaction wave is not affected by the dust particles, as only the driven part of the domain is seeded, and the rarefaction wave moves to the opposite side of the channel.

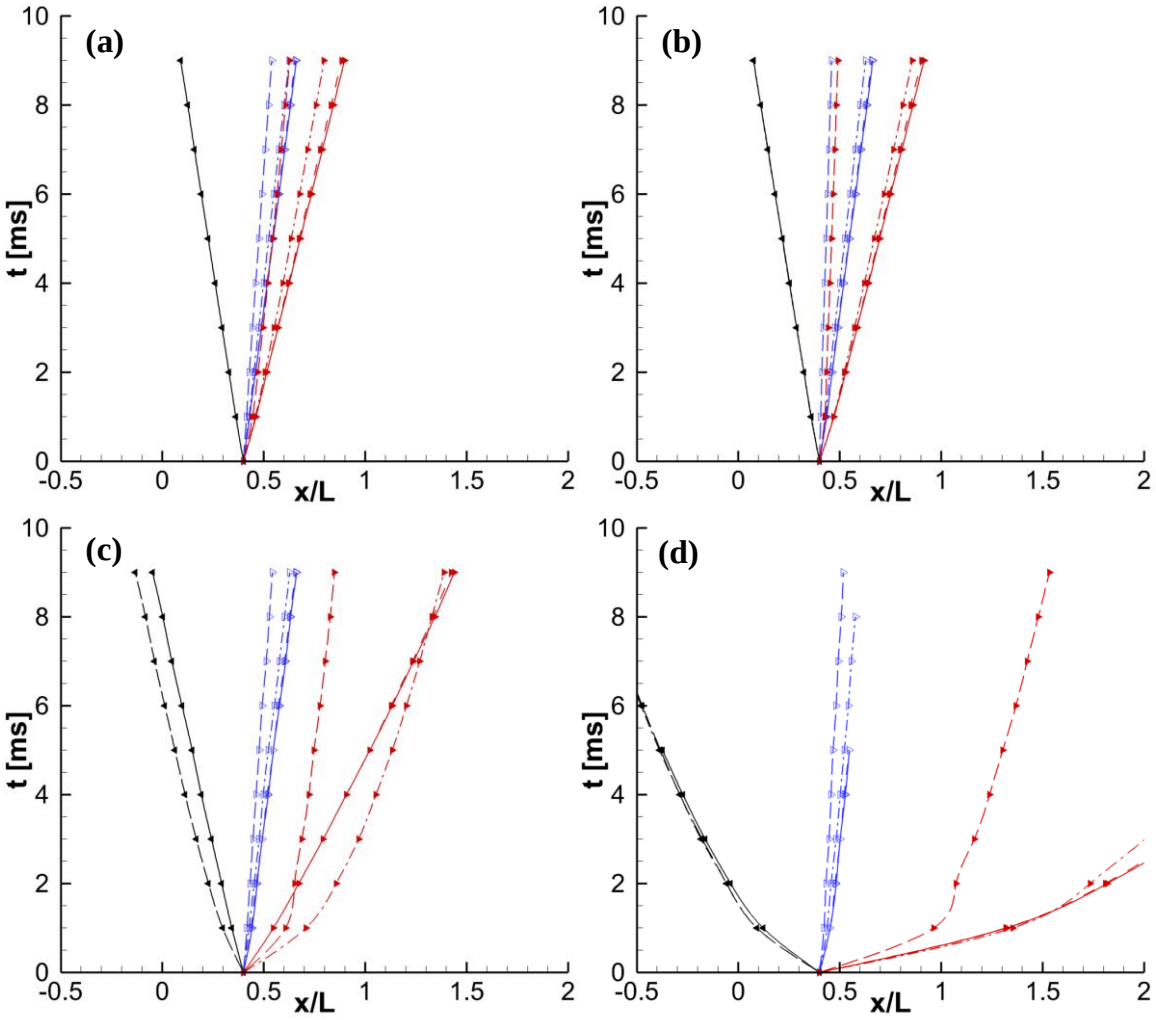

Fig. 14. Wave diagram of the shock wave and contact surface: (a) Kn = 0.0053; (b) Kn = 0.053; (c) Kn = 0.53; (d) Kn = 5.3. β = 0 (solid), β = 0.1 (dashed), β = 1 (dash-dot), β = 10 (long dash).

The effects of rarefaction on the complex wave patterns are investigated in Fig. 13 and Fig. 14. Here the Knudsen number is set to larger values by decreasing the gas phase pressure. It is worth noting that, to provide meaningful comparisons when the variation of Knudsen number is set by scaling the geometry size, the particle properties also should be modified in a way that the Stokes number (*St*) is kept constant. The Stokes number defines the level of interaction of gas and particles and is defined as the ratio of the relaxation time of the particles to the time scale of the fluid flow,[86]

$$St = \frac{\tau_V}{t_{ref}}. \tag{28}$$

Here t_{ref} is a reference time, which can be defined as the characteristic length divided by the characteristic speed, and τ_v is the momentum response time of the particles given by[86]

$$\tau_V = \frac{\rho_s d^2}{18\mu_g}. \tag{29}$$

In a flow with a small Stokes number (St<<1), the particulate phase will be in dynamic equilibrium with the carrier phase. On the other hand, in a larger Stokes number flow (St>>1), particles remain unaffected by the carrier phase, due to their large inertia. A summary of important parameters in gas-particle flows as well as the values used in these simulations is tabulated in Table II and Table III, respectively. However, in this study, the Knudsen number is modified by varying the initial pressure, and for comparison, we keep the particulate loading constant.

Table II. Summary of important parameters in gas-particle flows.

Term	Relation
Characteristic time	$t_{ref} = L_{ref} / \lvert \mathbf{u}_{ref} \rvert$
Particle momentum response time	$\tau_V = \rho_s d^2 / (18\mu_g)$
Stokes number	$St = \tau_V / t_{ref}$
Particulate loading	$\beta = \dot{m}_s / \dot{m}_g$
The physical interpretation of different Stokes regimes	
St << 1	$\tau_V << t_{ref}$: Enough time for particles to equilibrate (one-way coupling).
St >> 1	$\tau_V >> t_{ref}$: Particle velocity being little affected by the fluid velocity change, therefore remaining nearly equivalent velocities (two-way coupling).

- L_{ref} and $\mathbf{u}_{ref}$ represent the characteristic length and characteristic velocity, respectively.

- $\dot{m}_s$ and $\dot{m}_g$ denote particle mass flux and carrier phase mass flux, respectively.

Table III. Parameters used in simulations.

Parameter	Value
Carrier phase (Air)	
Pressure ratio	10
Temperature	300 (K)
Dynamic viscosity	2.23×10^{-5} (Pa·s)
Reference length	10 (m)
Reference velocity	321.95 (m/s)
Dispersed phase (glass bead)	
Particle diameter (d)	10 (μm)
Particulate loading (β)	0.1, 1, 10
Particle density	2500 (kg/m^3)

The corresponding Stokes number is 0.2112.

B. Needle-free injection case

To provide a better understanding of the governing physics of a dusty gas flow inside the non-invasive shock-powered powder injection technology, several simulations were designed to represent such devices in the presence of particles, walls, and non-equilibrium effects in two and three-dimensional space, and the results are discussed in this section.

1. Multidimensional flow inside micro shock tubes

In this subsection, the micro shock tube problem when particles are added to the flow is investigated. The studied setup is similar to the one analyzed in the IV.C.2 section for pure gas. A planar microchannel and a circular micropipe are considered and the two-phase equations of a dusty non-equilibrium gas are solved for two different Knudsen numbers. Particles with a diameter of 10μm and a density of 2500 kg/m^3 are added to the driven section of the channel. In all the simulations the NCCR model equipped with slip and temperature jump boundary conditions is solved for the gas phase. The particulate loading is set equal to 0.1 for all cases (i.e., lower particle concentration for the high Knudsen number case).

Even though the geometrical simplicity of this problem is far from the actual device, it can facilitate understanding the governing physics with more details. The actual design may include complexities such as shock entrance into the channels and under-expansion and impingement of the jet, which are briefly addressed in the following sections. The contours of normalized temperature, gas density, particle concentration, and Mach for two and three-dimensional setups for four different time steps are plotted in Fig. 15. In the figure, the top half contour corresponds to the pure gas and the bottom half represents the multiphase case for the three first quantities. In particle concentration contours, the upper and lower halves correspond to one-way and two-way coupled algorithms, respectively. As is evident from the comparison of the 2D and 3D contours, the contact and shock waves travel at a higher speed in planar channels compared to circular tubes. The rarefaction waves, however, travel at identical speeds in these geometries.

As expected, the shock front is decelerated because of the addition of particles. In the higher Knudsen case, the deceleration is magnified. The temperature and Mach variation are also much more limited in the rarefied case. The particle concentration contours reveal that, with a constant particulate loading, in a more rarefied flow, the distribution of particles is more uniform, and fewer particles are collected on the walls.

If Trehalose powder with a microscopic density of 1.58 g/cm^3 is filled in a tube with the current dimensions, the delivered dose will be around 70 ng, which is far below the target dose of injection in practice (≈1 mg), implying such a design is not suitable for this purpose. However, as this is a case that was previously studied (in single-phase flow) we continue our investigation for the sake of obtaining a physical understanding of the dynamics of the flow.

In most of the current designs, the dimensions of the channel are in the order of millimeters, with a driver pressure in the order of a few atmospheres. However, the current analysis is important not only because the physics of the interaction of non-equilibrium gases with particles is investigated in detail, but also because it can facilitate the emergence of new horizons in the advent of new designs. For example, the advantages that a high Knudsen number shock tube offers may motivate developing devices in which vacuum pumps are used to set the desired pressure ratio by keeping the device size constant. The other possible approach is to develop multi-nozzle devices to deliver the desired dose of the drug while keeping the device miniature in size with high driver pressure.

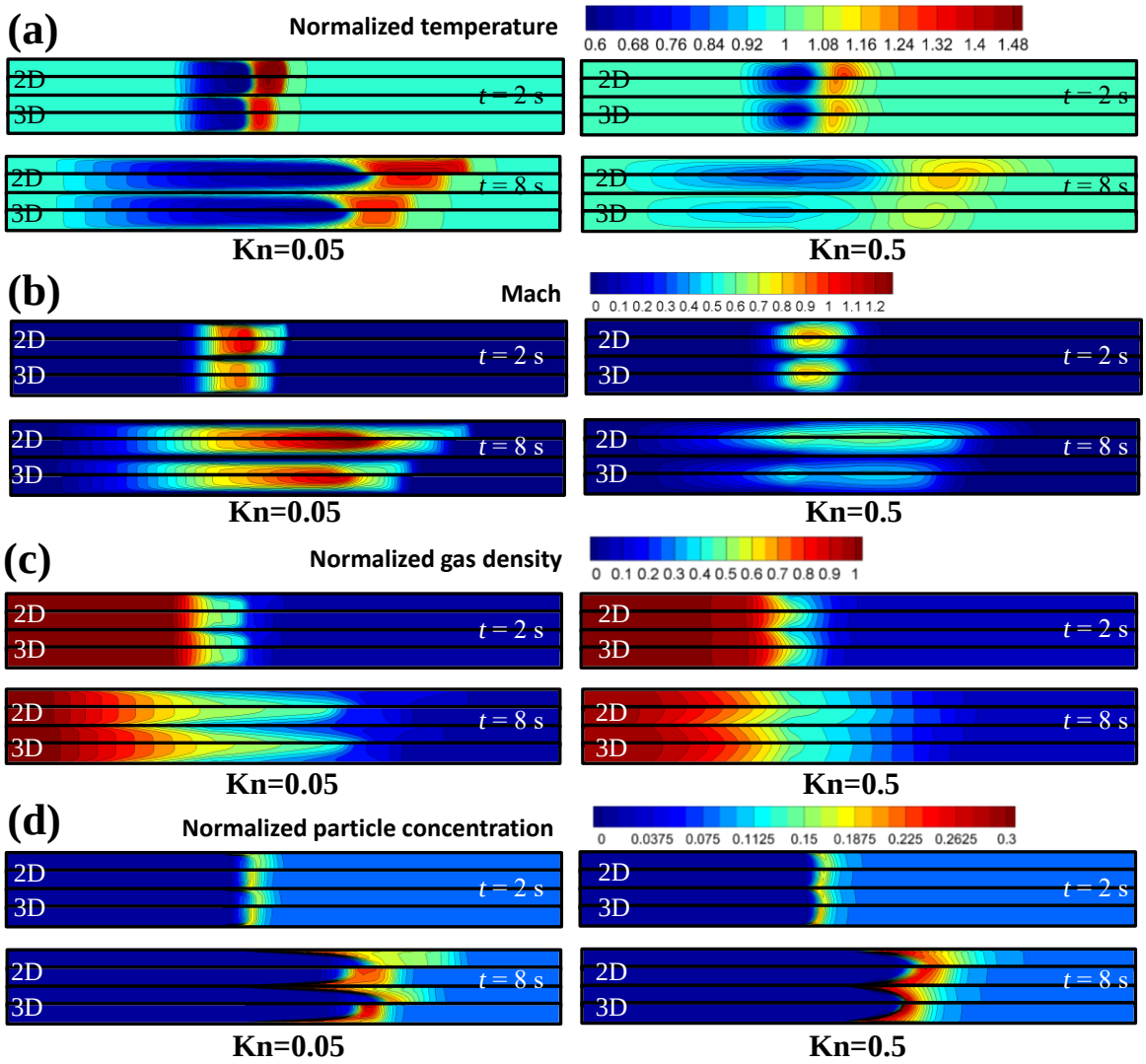

Fig. 15. A comparison of pure gas (upper half) and dusty gas (lower half) flow patterns inside a planar channel (2D) and circular pipe (3D) for different time steps. Temperature contours are normalized by the initial temperature, while the gas density and particle concentration contours are normalized by the initial density of the driver section.

2. Multiphase jet impingement on skin: drug delivery simulation

Even though our simulation of the jet impingement on the skin is limited to a few cases, potential designs with various operating conditions for different applications may be considered. A classification of regimes based on Mach and Knudsen numbers and an estimation of the margins of the potential operating range of a shock-powered powder needle-free drug delivery device are shown in Fig. 16. The classical models are valid only when the flow is in thermodynamic equilibrium. For slight deviation from continuum flow (up to early slip regime), the classical models equipped with velocity slip and temperature jump boundary conditions

can provide reliable results. However, further deviation from the equilibrium necessitates the application of high-order moments or particle-based approaches such as DSMC. Even though the low Knudsen number cases presented in this section can be simulated with classical models, the NCCR model was used for all the cases at the expense of slightly higher computational cost.

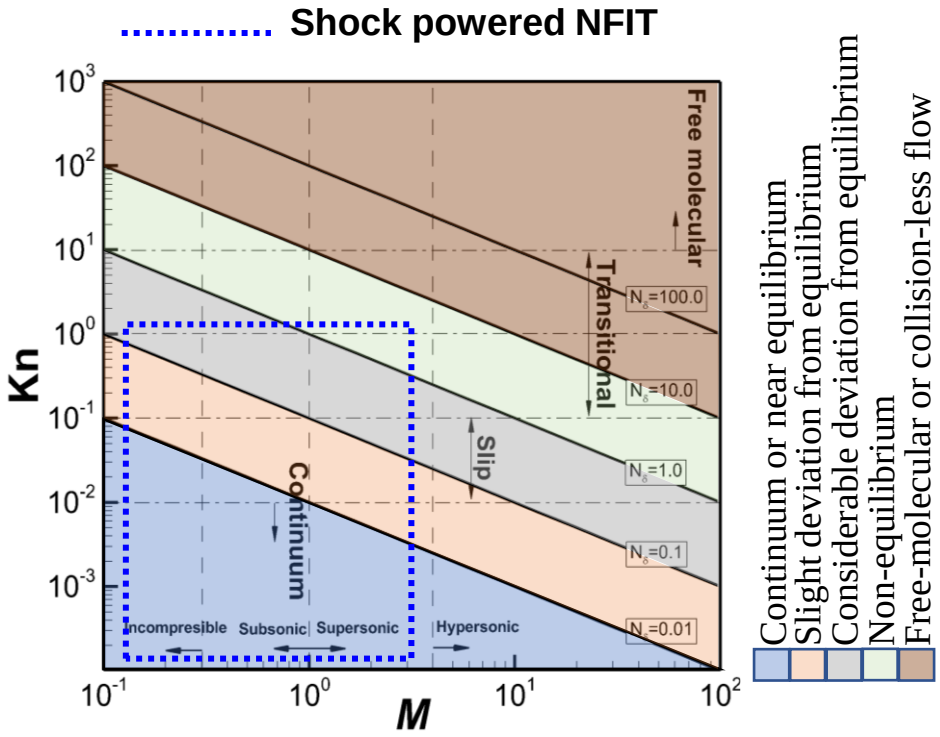

Fig. 16. Classification of degree of non-equilibrium based on Mach and Knudsen numbers and an approximation of operating condition of the needle-free drug delivery systems.

We simulated a case where a multiphase jet is expanded out of the tube, and the parametric studies on the Stokes number (via variation of the particle diameter) and the geometry (impingement height) are analyzed here. The schematic of the problem is shown in Fig. 17 (a).

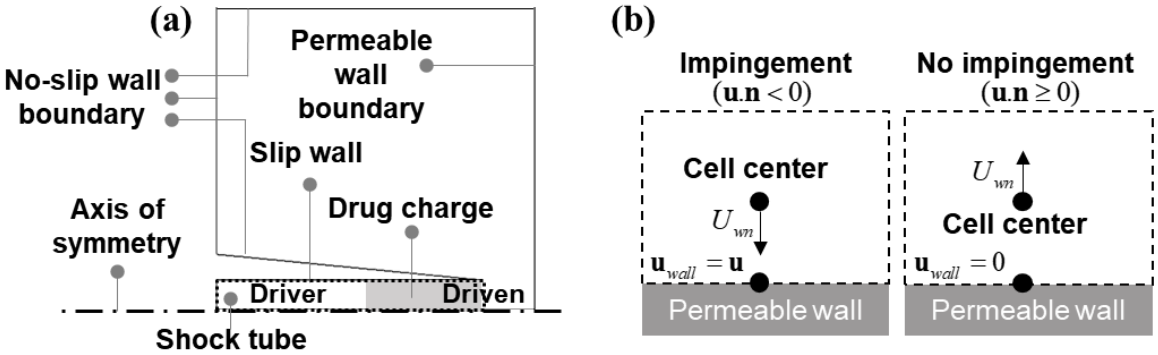

Fig. 17. (a) Schematic of the domain and (b) the concept of a permeable boundary condition for simulating drug impingement on a surface representing the skin.

The initial condition in the tube is the same as the cases studied in the previous section. The chamber located downstream has an initial condition identical to the driven section. The boundary conditions for both phases are identical except for the wall representing skin. For this boundary, a permeable wall boundary condition on the solid phase is applied. U_{wn} is the particle velocity component normal to the wall. When the particle velocity in an adjacent cell on the wall surface is positive and the projection of a normal vector on the solid surface is positive, the particles should not collide with the solid surface. This can be mathematically modeled as:

$$\begin{aligned} \mathbf{u}_{wall} &= 0 \quad if \quad \mathbf{u}\cdot\mathbf{n} \geq 0, \\ \mathbf{u}_{wall} &= \mathbf{u} \quad if \quad \mathbf{u}\cdot\mathbf{n} < 0. \end{aligned} \tag{30}$$

where **n** denotes the normal vector on the wall. The permeable wall boundary condition is illustrated in Fig. 17 (b). Furthermore, a zero-gradient (adiabatic) condition is imposed for the temperature values. The studied test cases are summarized in Table IV.

Table IV. Simulated test cases.

	Gas	Height (D*)	Kn	Diameter (μm)	Particulate loading
1	Argon	2	0.05	10	0.1
2		4			
3				5	
4				20	
5			0.1	10	0.1
6					0.2
7	Nitrogen				0.1
8					0.2

* D represents the channel exit diameter.

For the following cases, the Sutherland model of viscosity is applied:

$$\frac{\mu}{\mu_{ref}} = \left(\frac{T}{T_{ref}}\right)^{3/2} \frac{T_{ref} + S_{\mu}}{T + S_{\mu}}, \tag{31}$$

where, μ_{ref}, $T_{ref,}$ and S_{μ} are reference viscosity, temperature, and Sutherland constant, respectively.

Fig. 18 presents the time evolution of the propagation and impingement of particles on the surface, driven by the shock waves of two impingement heights when the carrier gas is argon.

Even though the geometry of the problem is simple, the physical phenomena occurring in this setup are rather complicated. After the diaphragm rupture, the dusty gas flow is expanded out of the channel impinging on the front surface and a stand-off shock wave is formed.

In the figure, the particle concentration and the velocity contours are plotted. When the impingement height is smaller, particles are collected on the surface sooner. Also, the concentration contours indicate that small fractions of particles can escape the permeable wall. These features are better quantified in the following figures.

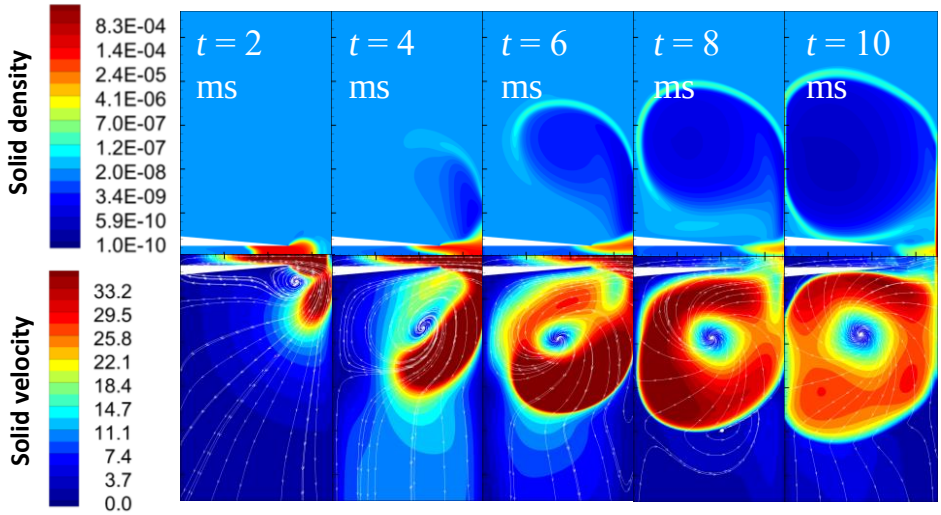

(a) Impingement height: 4D

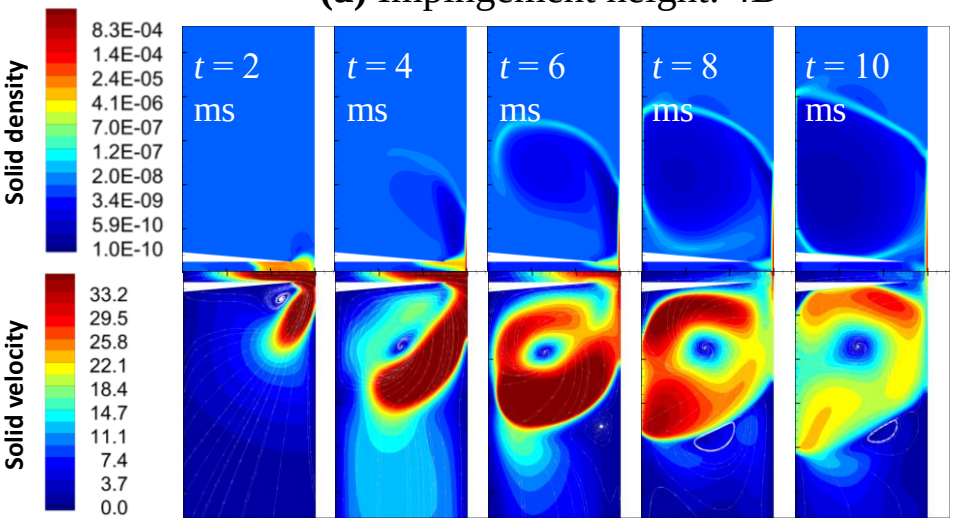

(b) Impingement height: 2D

Fig. 18. Parametric study on the impingement height, Kn = 0.05: (a) impingement height = 4D; (b) impingement height = 2D.

3. Analysis of collection efficiency in drug delivery simulation

We introduce a new concept, 'collection efficiency', which quantifies the efficiency of drug delivery in the two-phase jet impingement on skin. This parameter is defined as the normalized flux of the particles as follows:

$$\text{Collection efficiency} = \alpha_s \rho_s \mathbf{u} \cdot \mathbf{n} / \alpha_{s,ref} \rho_{s,ref} u_{ref} \ , \tag{32}$$

where subscript *ref* represents a reference value. Here the initial volume fraction, microscopic density, and speed of sounds are chosen for the $\alpha_{s,ref}$, $\rho_{s,ref,}$ and u_{ref} values, respectively. It should be noted that, unlike the air-droplet two-phase flow in atmospheric icing, where the reference is defined as a freestream value and the one-way coupling assumption is used,[66, 87] the present two-way coupling gas-particle flow with a reference defined as an initial value does not impose a maximum limit of 1 on collection efficiency.

In this context, this problem is not exactly simulating the injection process but is rather a simplification of the actual problem, providing a preliminary insight into how particles are convected and collected on the wall. In Fig. 19, the collection efficiency parameter is plotted on the permeable wall (representing skin) for two impingement heights. As can be seen in the profiles, the particles are collected on the skin as time passes. It can be observed that in the initial stages, there is no collection of particles on the wall boundary. As time passes by, particles impinge on the wall and then are carried out by the flow. When the impingement height is decreased to 2D, as shown in Fig. 19(b), particles are collected in the earlier stages. In addition, the maximum collection efficiency increases. It can be also observed that the peak of the collection efficiency curves is shifted away from the nozzle in the latest time steps investigated. Also, compared to the 4D impingement height, a wider area on the wall (skin) is exposed to the particle influx (approximately 3 cm exposure for 2D height compared to 2 cm for the 4D).

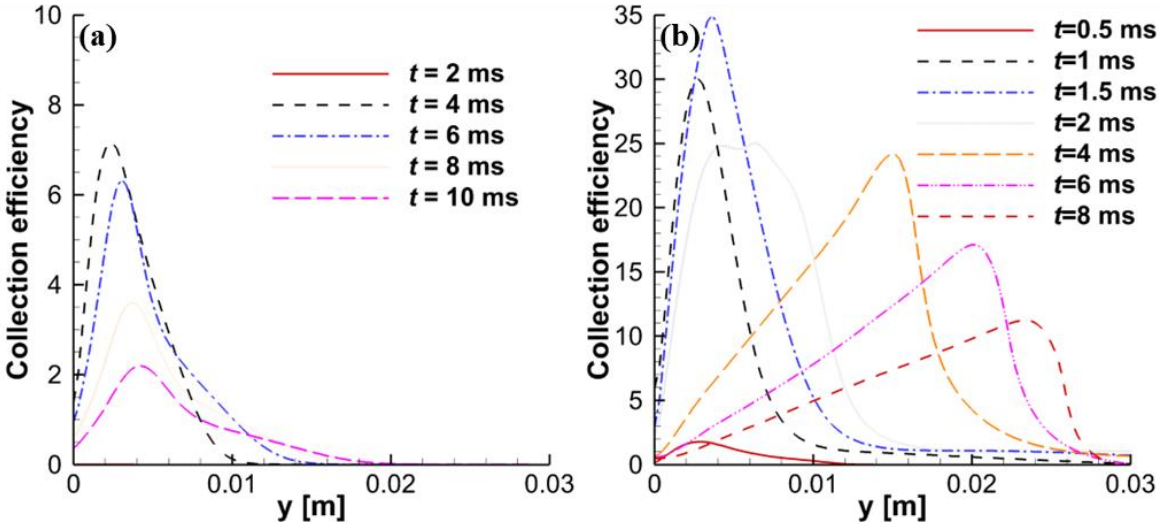

Fig. 19. Collection efficiency on the impinging surface, Kn = 0.05: (a) impingement height = 4D, (b) impingement height = 2D.

Fig. 20 shows a parametric study on the diameter of the particles for the case with an impingement height of 4D. In the figure, two particle diameters of 5 and 20 μm are investigated. Fig. 19(a) is the corresponding intermediate case d_p = 10 μm for this figure. When the particle diameter is small (small Stokes number), the particles closely follow the gas. Therefore, smaller particles are discharged much faster than large-diameter particles. However, as particles follow the gaseous flow, a portion of the discharge may not impinge on the surface. It can also be observed from the figure that the impingement area is wider (and more uniform) when smaller particles are used. The smaller particle diameters lead to a larger magnitude of collection efficiency.

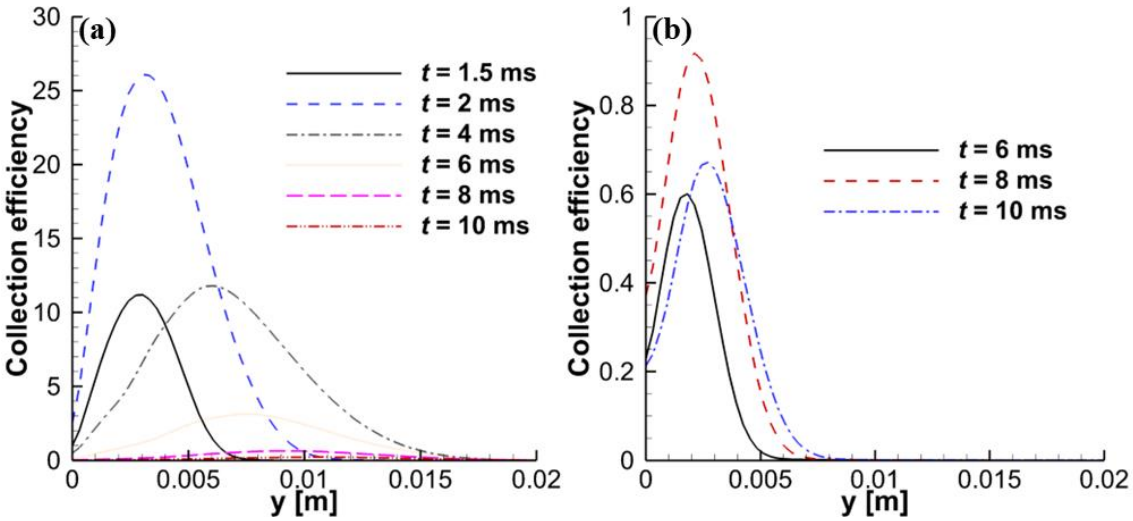

Fig. 20. Collection efficiency on the impinging surface, impingement height = 4D, Kn = 0.05: (a) d_p = 5 μm, (b) d_p = 20 μm.

In Fig. 21, the effect of variation of Knudsen number for monatomic argon and diatomic nitrogen gases is investigated. Two conditions were investigated. In the first scenario (first row), the Knudsen number is increased while the particulate loading is kept constant, meaning the density of the solid phase is halved as the Knudsen number is doubled. In the second scenario, only the Knudsen number is doubled, and the initial density of the solid phase is kept constant. To check how the increase affects the Knudsen number, Fig. 21(a) and Fig. 21(c) can be compared to Fig. 19(a). For both scenarios, the collection efficiency decreases with the increase in Knudsen number. For nitrogen gas, which has a bulk viscosity of 0.8, the collection efficiency decreases. However, the trends of accumulation of particles are the same for both gases. Also, as the Knudsen increases, the collection of particles is faster. The collection trends for all the investigated cases were almost identical, however, in the high Knudsen number case, the distribution was more uniform.

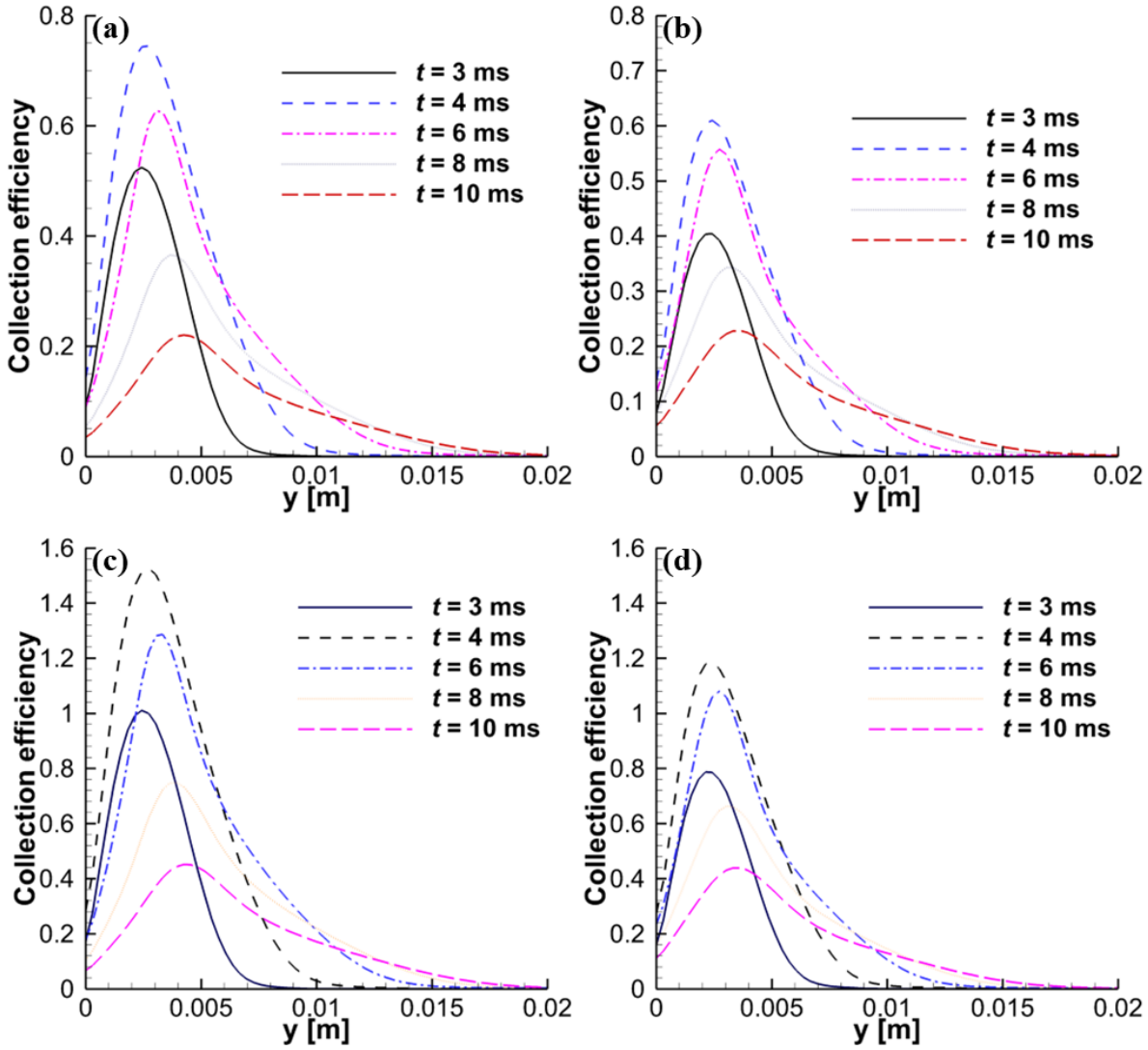

Fig. 21. Rarefaction effects on collection efficiency, top row: Kn = 0.1, ρs = ρref/2, (a) argon; (b) nitrogen, bottom row: Kn = 0.1, ρs = ρref, (c) argon; (d) nitrogen.

4. Analysis of vorticity growth rates in the two-phase jet impingement problem

The vorticity growth rates in the multiphase jet impingement problem were also analyzed. The well-known vorticity transport equation (VTE) for inviscid compressible flow reads as:

$$\frac{D\boldsymbol{\omega}}{Dt} = (\boldsymbol{\omega}\cdot\nabla)\mathbf{u} - \boldsymbol{\omega}(\nabla\cdot\mathbf{u}) + \frac{1}{\rho^2}\nabla\rho\times\nabla p\,. \tag{33}$$

Recently a new vorticity transport equation which includes viscous terms and abandons Stokes' hypothesis has been derived for diatomic and polyatomic gases.[88] Based on this derivation, the

new VTE of the Navier-Fourier equation for gas (or solid) in a two-phase flow can be easily derived. The momentum equation reads as:

$$\frac{\partial \mathbf{u}}{\partial t} = -(\mathbf{u}\cdot\nabla)\mathbf{u} - \frac{1}{\hat{\rho}}\nabla p + \frac{1}{\hat{\rho}}\nabla\cdot\left[\mu\left(2\left[\nabla\mathbf{u}\right]^{(2)} + f_b(\nabla\cdot\mathbf{u})\mathbf{I}\right)\right] + \frac{D}{\hat{\rho}}(\mathbf{u}_S - \mathbf{u}) \tag{34}$$

where $\hat{\rho} \equiv \alpha\rho$. This will yield

$$\begin{aligned}
\frac{D\boldsymbol{\omega}}{Dt} &= (\boldsymbol{\omega}\cdot\nabla)\mathbf{u} - \boldsymbol{\omega}(\nabla\cdot\mathbf{u}) + \frac{\mu}{\hat{\rho}}\nabla^2\boldsymbol{\omega} \\
&+ \frac{1}{\hat{\rho}^2}\nabla\hat{\rho}\times\nabla p - \frac{\mu}{\hat{\rho}^2}\nabla\hat{\rho}\times\nabla^2\mathbf{u} - \left(\frac{1}{3} + f_b\right)\frac{\mu}{\hat{\rho}^2}\nabla\hat{\rho}\times\nabla(\nabla\cdot\mathbf{u}) \\
&+ \frac{1}{\hat{\rho}}(\nabla\mu\cdot\nabla)\boldsymbol{\omega} + \frac{1}{\hat{\rho}}(\boldsymbol{\omega}\cdot\nabla)\nabla\mu - \frac{\boldsymbol{\omega}}{\hat{\rho}}\nabla^2\mu + \frac{1}{\hat{\rho}}\nabla\mu\times\nabla^2\mathbf{u} + \frac{2}{\hat{\rho}}\nabla(\nabla\mu\cdot\nabla)\times\mathbf{u} \\
&- \frac{1}{\hat{\rho}^2}\nabla\hat{\rho}\times(\nabla\mu\times\boldsymbol{\omega}) - \frac{2}{\hat{\rho}^2}\nabla\hat{\rho}\times(\nabla\mu\cdot\nabla)\mathbf{u} + \left(\frac{2}{3} - f_b\right)\frac{(\nabla\cdot\mathbf{u})}{\hat{\rho}^2}\nabla\hat{\rho}\times\nabla\mu \\
&+ \frac{1}{\hat{\rho}}\nabla\mu\times\nabla(\nabla\cdot\mathbf{u}) + \frac{D}{\hat{\rho}}(\nabla\times\mathbf{u}_S - \boldsymbol{\omega}) + \nabla\left(\frac{D}{\hat{\rho}}\right)\times(\mathbf{u}_S - \mathbf{u}).
\end{aligned} \tag{35}$$

The corresponding equation for NCCR can be calculated as follows:

$$\begin{aligned}
\frac{D\boldsymbol{\omega}}{Dt} &= (\boldsymbol{\omega}\cdot\nabla)\mathbf{u} - \boldsymbol{\omega}(\nabla\cdot\mathbf{u}) + \frac{1}{\hat{\rho}^2}\nabla\hat{\rho}\times\nabla(p+\Delta) - \nabla\times\left(\frac{\nabla\cdot\boldsymbol{\Pi}}{\hat{\rho}}\right) + \frac{D}{\hat{\rho}}(\nabla\times\mathbf{u}_S - \boldsymbol{\omega}) \\
&+ \nabla\left(\frac{D}{\hat{\rho}}\right)\times(\mathbf{u}_S - \mathbf{u}).
\end{aligned} \tag{36}$$

The viscous stress term in NCCR cannot be further simplified, since it is not a linear function of the velocity gradient.

The terms in the right-hand side of the equation (36) from right to left are the stretching term (which is the lengthening of vortices in a three-dimensional fluid flow, associated with a corresponding increase in the vorticity component in the stretching direction) which is an important mechanism in the dynamics of turbulence, the dilatation term (responsible for the fluid convection and thermal expansion, which remains important in highly compressible fluids), the baroclinicity term (a measure of how misaligned the gradient of the sum of pressure and excess normal stress is from the gradient of density in a fluid) which is responsible for the production of small-scale rolled up vortices at different density interfaces, and the viscous term (due to presence of viscosity). The last two terms are named multiphase terms (due to the presence of a relative velocity between the two phases). To provide a qualitative understanding

of the behavior of each term the time evolutions of these parameters are provided in Fig. 22. The vortical structures emerge near the channel walls and at the channel exit. The baroclinicity, dilatation, and viscous terms are dominant at the channel exit just before the flow is expanded. The multiphase term is dominant inside the channel where particles are initially seeded, and it is propagated with the path of particle propagation.

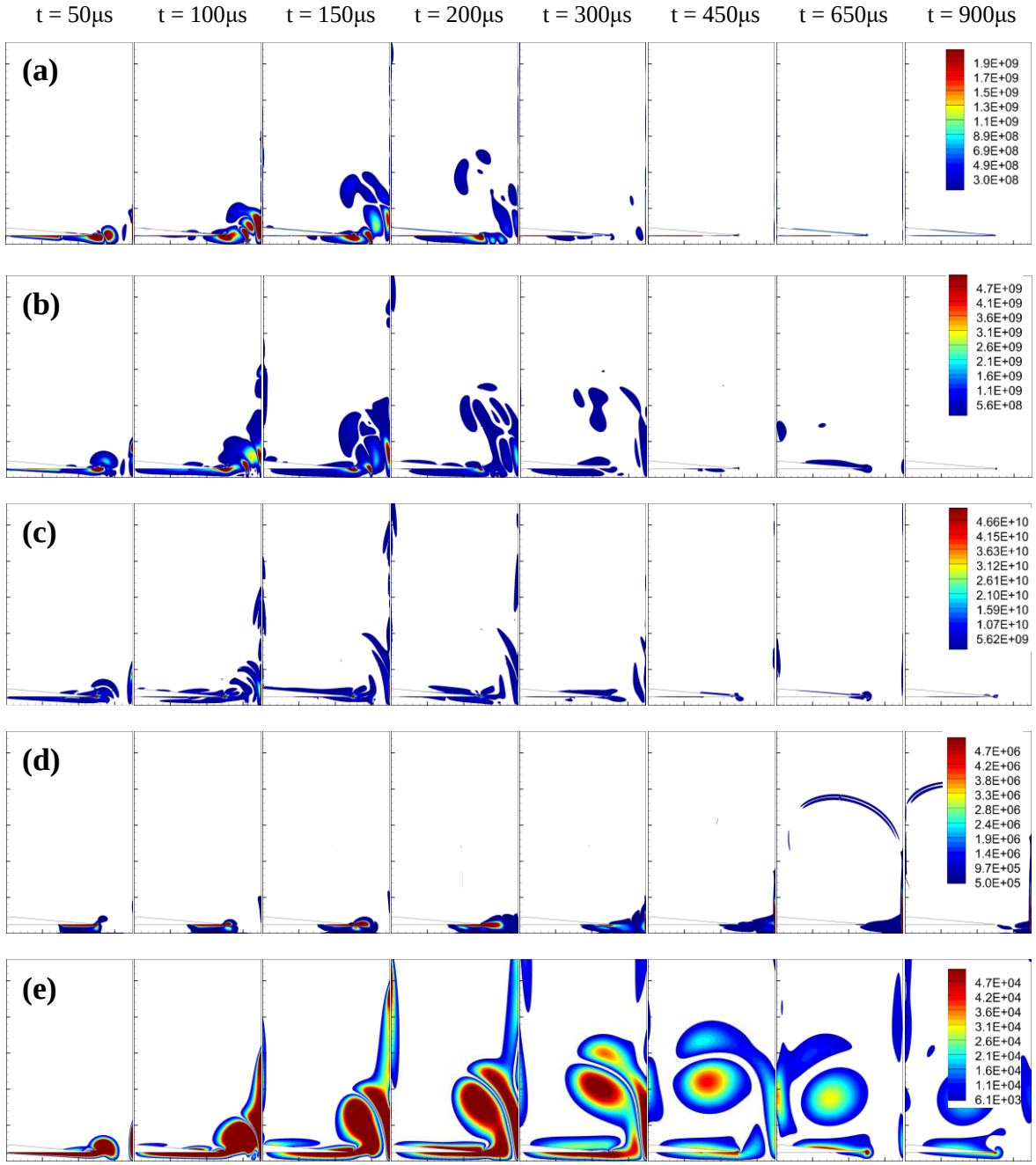

Fig. 22. Time evolution of the terms in the vorticity transport equation: (a) baroclinicity; (b) dilatation; (c) viscous; (d) multiphase; and (e) vorticity.

For a more quantitative understanding of the effect of these terms, the following spatial integrations are defined:

$$\left|\boldsymbol{\omega}_{stretching}\right|(t)=\int_D\left|(\boldsymbol{\omega}\cdot\nabla)\mathbf{u}\right|dxdy\,, \tag{37}$$

$$\left|\boldsymbol{\omega}_{dilatation}\right|(t)=-\int_D\left|\boldsymbol{\omega}(\nabla\cdot\mathbf{u})\right|dxdy\,, \tag{38}$$

$$\left|\boldsymbol{\omega}_{baroclinicity}\right|(t)=\int_D\left|\frac{1}{\hat{\rho}^2}\nabla\hat{\rho}\times\nabla(p+\Delta)\right|dxdy\,, \tag{39}$$

$$\left|\boldsymbol{\omega}_{viscous}\right|(t)=\int_D\left|\nabla\times\left(\frac{\nabla\cdot\boldsymbol{\Pi}}{\hat{\rho}}\right)\right|dxdy\,, \tag{40}$$

$$\left|\boldsymbol{\omega}_{multiphase}\right|(t)=\int_D\left|\frac{D}{\hat{\rho}}(\nabla\times\mathbf{u}_S-\boldsymbol{\omega})+\nabla\left(\frac{D}{\hat{\rho}}\right)\times(\mathbf{u}_S-\mathbf{u})\right|dxdy\,. \tag{41}$$

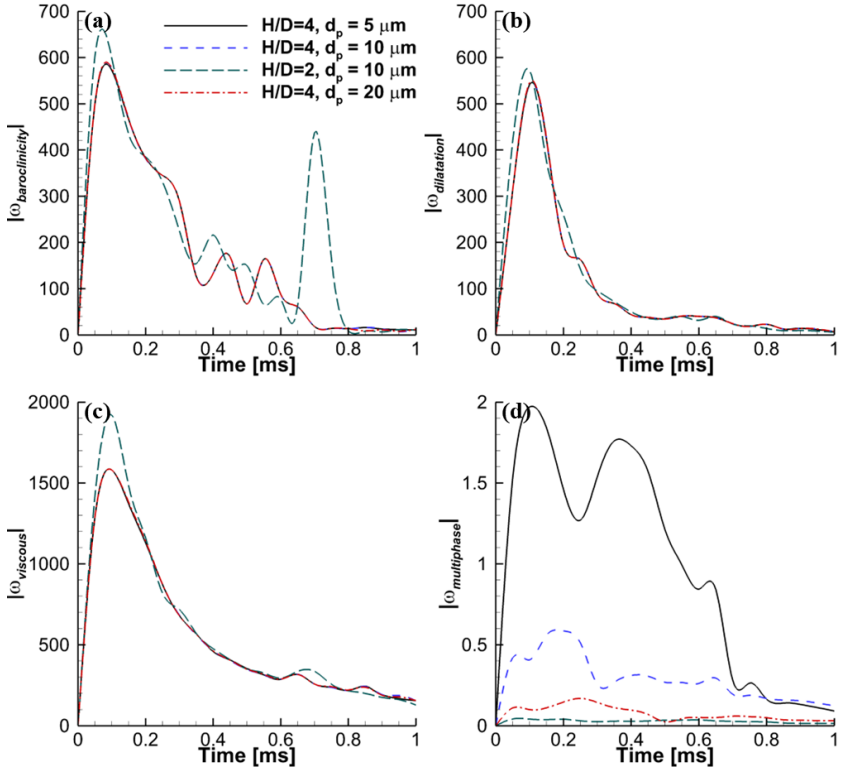

Fig. 23. The effect of varying impingement height and particle diameter on the growth rate of various terms in the VTE: (a) baroclinicity; (b) dilatation; (c) viscous; (d) multiphase.

In Fig. 23, the evolution of these parameters (except for the stretching term, since the flow is two-dimensional) is investigated for 4 cases (effect of variation of diameter and height). The

effects of varying particle diameter on the growth rates of the four mechanisms of baroclinicity, dilatation, viscous, and multiphase are plotted. As observed in the figure, the particle diameter has a negligible effect on all the vorticity growth rates except for the multiphase term. A smaller diameter particle contributes more to the multiphase term. Also, the contribution of the multiphase term is almost negligible compared to the other three terms. All the terms experience a sudden increase followed by a gradual decrease as time passes. This sudden jump corresponds to the time when the flow is expanded out of the channel. It was also observed that all the terms reach larger values when the impingement height is shorter (except for the multiphase term).

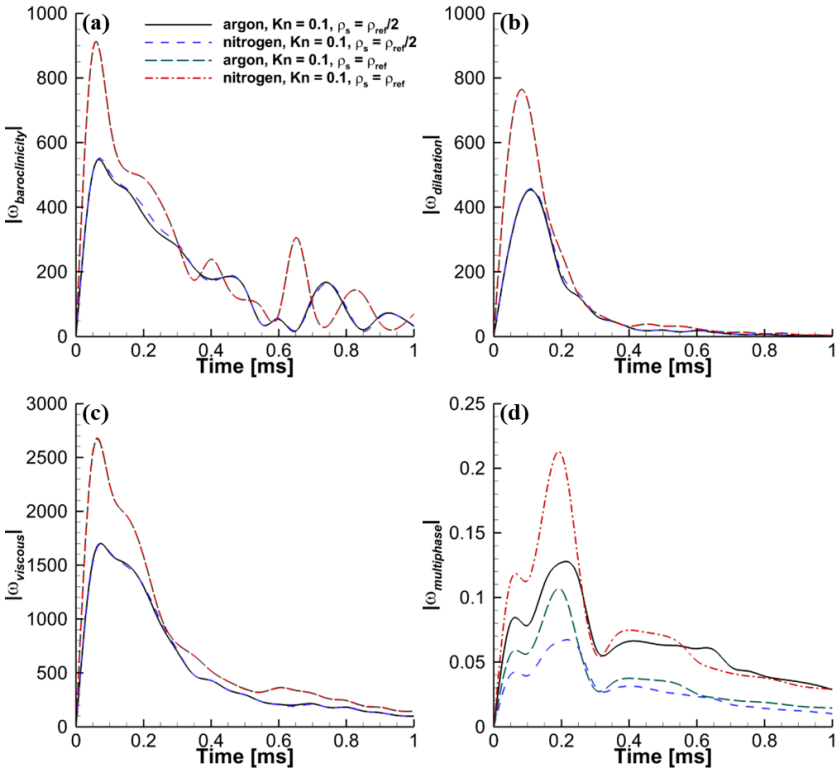

Fig. 24. Vorticity growth rates for two different gases and two different scenarios when the Knudsen number is increased: (a) baroclinicity; (b) dilatation; (c) viscous; (d) multiphase.

Fig. 24 investigates the effect of various vorticity growth rates for the two scenarios discussed in the previous subsection for two gases. As can be observed, the vorticity growth rates have identical behaviors for both simulated gases. The only term that is significantly affected by the variation in gas is the multiphase term, as can be seen in Fig. 24 (d). Comparing Fig. 24 and Fig. 23 reveals that by increasing the Knudsen number the magnitude of the vorticity terms in the VTE increases for all the investigated mechanisms except for the

multiphase term. It was also observed that in the second scenario (where the initial drug dose is doubled compared to the first scenario), the vorticity growth rates increased as well.

VI. CONCLUSIONS

In the present work, conservation laws along with the appropriate constitutive models were implemented and solved to help improve the understanding of the governing physics that are important in a specific class of needle-free drug delivery systems (i.e., shock-powered powder injection). As the wave diagrams of a single-phase and two-phase shock tube illustrated, both non-equilibrium effects and the addition of particles lead to non-linear behavior in shock movement, which is not present in classical shock tube problems. It was also demonstrated that among needle-free drug delivery devices with non-equilibrium effects, the deviation between the first-order and second-order theories can be considerable. The applied NCCR model outperformed the NSF model, providing solutions more identical to DSMC. An interesting feature of the high Knudsen number case was the placement of all three discontinuities of the Sod problem in one place.

The investigation of bulk viscosity effects also revealed some interesting features, including the non-linear and non-monotone behaviors (e.g., an increase and decrease in maximum Mach number) as the f_b was increased, and the formation of a steep change in properties followed by a thick relaxation zone to reach equilibrium with the downstream (also known as a double-layer shock structure). These effects were magnified when the Knudsen number increased. It was also demonstrated that such patterns can only be captured once a higher-order model (NCCR) is used. Even after abandoning the Stokes hypothesis, the linear theory is incapable of resolving the correct features.

The flow problem was investigated for multi-dimensional test cases and similar results were confirmed. In multidimensional problems, a boundary layer resulting from the presence of a wall can affect the dynamics of the flow. It was also observed that when Maxwell velocity slip and Smoluchowski temperature jump boundary conditions were applied, both the NSF and NCCR theories showed good agreement for Knudsen numbers as high as 0.53, however, a further increase of Knudsen number led to model deviations.

A comparison of 2D and 3D geometries revealed that the contact and shock waves travel at a higher speed in planar channels compared to circular tubes. The rarefaction waves, however, travel at identical speeds in these geometries. It was also observed that, with constant

particulate loading, in a more rarefied flow, the distribution of the particles is more uniform, and fewer particles collect on the walls.

Then, test cases representing a needle-free device were designed and simulated to show how rarefaction and particle diameter can affect the collection of particles on an impinging wall, which is representative of skin. It was shown that when the impingement height is decreased to half the height of the original case, particles are collected on the skin in the earlier stages, and the maximum collection efficiency is increased. The peak of the collection efficiency curves shifted away from the nozzle in the latest time steps investigated. Furthermore, a wider area on the wall (skin) was exposed to the particle influx (approximately 3 cm exposure for 2D height compared to 2 cm for the 4D). A comparison of different particle diameters indicated that when the particle diameter was small (small Stokes number), the discharge occurred at a faster rate compared to large-diameter particles. Moreover, as particles followed the gaseous flow, a portion of the discharge may not impinge on the surface, and the impingement area is wider (and more uniform) in this case. The analysis of rarefaction effects showed that the collection efficiency decreases with the increase in Knudsen number, however, a more uniform distribution is obtained at high-Knudsen flows. For nitrogen gas, which has a bulk viscosity ratio of 0.8, the collection efficiency is lower compared to argon gas. However, the trends of particle accumulation were the same for both gases.

In addition, a new equation for the vorticity growth rates for a two-phase flow of gas and solid particles was derived, and the contribution of each term to the evolution of vortical structures in the latter problem was discussed. It was found that the thermophysical properties of the investigated gases, as well as the particle diameter, have a negligible effect on the vortical growth rates.

The present study can be extended by conducting further parametric studies on the geometry of the tubes, simulation of the powder penetration into the skin (porous medium simulation), the addition of granular flow models based on the kinetic theory of granular flow (KTGF), and by investigating the shock entrance into the channel.

ACKNOWLEDGMENTS

This work was supported by the National Research Foundation of Korea grants funded by the Ministry of Science and ICT (NRF 2022R1I1A1A01065532 and NRF 2022R1A4A1030333), South Korea. R.S.M. acknowledges the support from the National

Research Foundation of Korea funded by the Ministry of Science and ICT (NRF 2017-R1A5A1015311).

APPENDIX: DERIVATION OF THE VISCOUS COMPRESSIBLE VORTICITY TRANSPORT EQUATION OF A TWO-PHASE FLOW INCLUDING BULK VISCOSITY

We consider two-phase flows of monatomic, diatomic, and polyatomic gases with considerable variations in temperature in the flow fields, interacting with solid particles. Since we are dealing with diatomic and polyatomic gases, we abandon Stokes' hypothesis, resulting in the following compressible version of the momentum equation with transport coefficients dependent on the temperature,

$$\frac{\partial(\hat{\rho}\mathbf{u})}{\partial t}+\nabla\cdot\left(\hat{\rho}\mathbf{u}\mathbf{u}+p\mathbf{I}\right)-\nabla\cdot\left(2\mu\left[\nabla\mathbf{u}\right]^{(2)}+\mu_b(\nabla\cdot\mathbf{u})\mathbf{I}\right)=D(\mathbf{u}_s-\mathbf{u}). \tag{A1}$$

The corresponding viscous compressible vorticity equation for flows of diatomic and polyatomic gases, after lengthy derivation, can be summarized as,

$$\begin{aligned}
\frac{D\boldsymbol{\omega}}{Dt}&=(\boldsymbol{\omega}\cdot\nabla)\mathbf{u}-\boldsymbol{\omega}(\nabla\cdot\mathbf{u})+\frac{\mu}{\hat{\rho}}\nabla^2\boldsymbol{\omega}\\
&+\frac{1}{\hat{\rho}^2}\nabla\hat{\rho}\times\nabla p-\frac{\mu}{\hat{\rho}^2}\nabla\hat{\rho}\times\nabla^2\mathbf{u}-\left(\frac{1}{3}+f_b\right)\frac{\mu}{\hat{\rho}^2}\nabla\hat{\rho}\times\nabla(\nabla\cdot\mathbf{u})\\
&+\frac{1}{\hat{\rho}}(\nabla\mu\cdot\nabla)\boldsymbol{\omega}+\frac{1}{\hat{\rho}}(\boldsymbol{\omega}\cdot\nabla)\nabla\mu-\frac{\boldsymbol{\omega}}{\hat{\rho}}\nabla^2\mu+\frac{1}{\hat{\rho}}\nabla\mu\times\nabla^2\mathbf{u}+\frac{2}{\hat{\rho}}\nabla(\nabla\mu\cdot\nabla)\times\mathbf{u}\\
&-\frac{1}{\hat{\rho}^2}\nabla\hat{\rho}\times(\nabla\mu\times\boldsymbol{\omega})-\frac{2}{\hat{\rho}^2}\nabla\hat{\rho}\times(\nabla\mu\cdot\nabla)\mathbf{u}+\left(\frac{2}{3}-f_b\right)\frac{(\nabla\cdot\mathbf{u})}{\hat{\rho}^2}\nabla\hat{\rho}\times\nabla\mu+\frac{1}{\hat{\rho}}\nabla\mu\times\nabla(\nabla\cdot\mathbf{u})\\
&+\frac{D}{\hat{\rho}}(\nabla\times\mathbf{u}_S-\boldsymbol{\omega})+\nabla\left(\frac{D}{\hat{\rho}}\right)\times(\mathbf{u}_S-\mathbf{u}).
\end{aligned} \tag{A2}$$

This is a new equation, whose derivation (without considering the two-phase terms) can be found in the appendix of Singh *et al.*[88]. In this appendix, we provide the full derivation including the two-phase terms for completeness. In the above equation, the second line is $\nabla\hat{\rho}$ related, the third line is $\nabla\mu$ related, and the fourth line is $\nabla\hat{\rho}$ (or $\nabla(\nabla\cdot\mathbf{u})$) and $\nabla\mu$ related. There are two terms associated with bulk viscosity $-f_b\left[\mu\nabla\hat{\rho}\times\nabla(\nabla\cdot\mathbf{u})+(\nabla\cdot\mathbf{u})\nabla\hat{\rho}\times\nabla\mu\right]/\hat{\rho}^2$ and two terms associated with multiphase source terms $\frac{D}{\hat{\rho}}(\nabla\times\mathbf{u}_S-\boldsymbol{\omega})+\nabla\left(\frac{D}{\hat{\rho}}\right)\times(\mathbf{u}_S-\mathbf{u})$.

The detailed derivation of (A2) from (A1) can be summarized as follows. The conservation law of momentum can be rewritten as

$$\begin{aligned}&\frac{\partial \mathbf{u}}{\partial t} = -(\mathbf{u}\cdot\nabla)\mathbf{u} - \frac{1}{\hat{\rho}}\nabla p + \frac{1}{\hat{\rho}}\nabla\cdot\left(2\mu\left[\nabla\mathbf{u}\right]^{(2)} + \mu_b(\nabla\cdot\mathbf{u})\mathbf{I}\right) + \frac{1}{\hat{\rho}}D(\mathbf{u}_s - \mathbf{u}),\\ &\text{Or } \frac{\partial \mathbf{u}}{\partial t} = -(\mathbf{u}\cdot\nabla)\mathbf{u} - \frac{1}{\hat{\rho}}\nabla p + \frac{1}{\hat{\rho}}\nabla\cdot\left[\mu\left(2\left[\nabla\mathbf{u}\right]^{(2)} + f_b(\nabla\cdot\mathbf{u})\mathbf{I}\right)\right] + \frac{1}{\hat{\rho}}D(\mathbf{u}_s - \mathbf{u}).\end{aligned} \tag{A3}$$

Using a relation

$$2\left[\nabla\mathbf{u}\right]^{(2)} \equiv \left(\nabla\mathbf{u}^T + \nabla\mathbf{u}\right) - \frac{2}{3}(\nabla\cdot\mathbf{u})\mathbf{I} = 2\nabla\mathbf{u}^T + \text{tensor}\{\boldsymbol{\omega}\} - \frac{2}{3}(\nabla\cdot\mathbf{u})\mathbf{I}, \tag{A4}$$

we can show

$$\begin{aligned}\frac{1}{\hat{\rho}}\nabla\cdot\left(2\mu\left[\nabla\mathbf{u}\right]^{(2)}\right) &= \frac{1}{\hat{\rho}}\nabla\cdot\left[2\mu\nabla\mathbf{u}^T + \mu\ \text{tensor}\{\boldsymbol{\omega}\} - \frac{2}{3}\mu(\nabla\cdot\mathbf{u})\mathbf{I}\right]\\ &= \frac{1}{\hat{\rho}}\left[2\nabla\cdot\left(\mu\nabla\mathbf{u}^T\right) + \nabla\cdot\left(\mu\ \text{tensor}\{\boldsymbol{\omega}\}\right) - \frac{2}{3}\nabla\left(\mu(\nabla\cdot\mathbf{u})\right)\right]\\ &= \frac{1}{\hat{\rho}}\left[2\nabla\cdot\left(\mu\nabla\mathbf{u}^T\right) + \nabla\times\left(\mu\boldsymbol{\omega}\right) - \frac{2}{3}\nabla\left(\mu(\nabla\cdot\mathbf{u})\right)\right],\\ \frac{1}{\hat{\rho}}\nabla\cdot\left(f_b\mu(\nabla\cdot\mathbf{u})\mathbf{I}\right) &= \frac{f_b}{\hat{\rho}}\nabla\left(\mu(\nabla\cdot\mathbf{u})\right)\end{aligned} \tag{A5}$$

and

$$\begin{aligned}\frac{\partial \mathbf{u}}{\partial t} = &-(\mathbf{u}\cdot\nabla)\mathbf{u} - \frac{1}{\hat{\rho}}\nabla p + \frac{2}{\hat{\rho}}\nabla\cdot\left(\mu\nabla\mathbf{u}^T\right) + \frac{1}{\hat{\rho}}\nabla\times\left(\mu\boldsymbol{\omega}\right) + \frac{1}{\hat{\rho}}\left(f_b - \frac{2}{3}\right)\nabla\left(\mu(\nabla\cdot\mathbf{u})\right)\\ &+ \frac{1}{\hat{\rho}}D(\mathbf{u}_s - \mathbf{u}).\end{aligned} \tag{A6}$$

Using the following identities for a scalar ϕ, a vector $\mathbf{A}$, a tensor $\mathbf{T}$,

$$\begin{aligned}&\nabla\cdot(\phi\mathbf{A}) = \phi\nabla\cdot\mathbf{A} + \mathbf{A}\cdot\nabla\phi,\ \nabla\cdot(\phi\mathbf{T}) = \phi\nabla\cdot\mathbf{T} + \nabla\phi\cdot\mathbf{T},\\ &\nabla\times(\phi\mathbf{A}) = \phi\nabla\times\mathbf{A} + \nabla\phi\times\mathbf{A},\ \nabla\times(\nabla\times\mathbf{A}) = \nabla(\nabla\cdot\mathbf{A}) - \nabla^2\mathbf{A},\end{aligned}$$

we obtain

$$\nabla\cdot\left(\mu\nabla\mathbf{u}^{T}\right)=\left(\nabla\mu\cdot\nabla\right)\mathbf{u}+\mu\nabla^{2}\mathbf{u},$$
$$\nabla\times\left(\mu\boldsymbol{\omega}\right)=\mu\nabla\times\boldsymbol{\omega}+\nabla\mu\times\boldsymbol{\omega}=\mu\nabla\left(\nabla\cdot\mathbf{u}\right)-\mu\nabla^{2}\mathbf{u}+\nabla\mu\times\boldsymbol{\omega}. \tag{A7}$$

Then (A6) can be rewritten as

$$\frac{\partial\mathbf{u}}{\partial t}=-\left(\mathbf{u}\cdot\nabla\right)\mathbf{u}-\frac{1}{\hat{\rho}}\nabla p+\frac{\mu}{\hat{\rho}}\nabla^{2}\mathbf{u}+\frac{2}{\hat{\rho}}\left(\nabla\mu\cdot\nabla\right)\mathbf{u}+\frac{1}{\hat{\rho}}\nabla\mu\times\boldsymbol{\omega}+\frac{\mu}{\hat{\rho}}\nabla\left(\nabla\cdot\mathbf{u}\right)$$
$$+\frac{1}{\hat{\rho}}\left(f_{b}-\frac{2}{3}\right)\nabla\left(\mu\left(\nabla\cdot\mathbf{u}\right)\right)+\frac{1}{\hat{\rho}}D(\mathbf{u}_{s}-\mathbf{u}). \tag{A8}$$

Finally, we can derive the viscous compressible vorticity equation (A2) by taking the $\nabla\times$ of each term. The first to eighth terms can be derived in the same way as described in the appendix of Singh *et al.*[88].

The ninth term:

$$\nabla\times\left[\frac{1}{\hat{\rho}}D(\mathbf{u}_{s}-\mathbf{u})\right]=\frac{D}{\hat{\rho}}\left(\nabla\times\mathbf{u}_{S}-\boldsymbol{\omega}\right)+\nabla\left(\frac{D}{\hat{\rho}}\right)\times\left(\mathbf{u}_{S}-\mathbf{u}\right).$$

REFERENCES

[1]R. E. Duff, "Shock-tube performance at low initial pressure," The Physics of Fluids **2**, 207 (1959).

[2]H. Mirels, "Test time in low-pressure shock tubes," The Physics of Fluids **6**, 1201 (1963).

[3]S. Tüchler, and C. D. Copeland, "Numerical optimisation of a micro-wave rotor turbine using a quasi-two-dimensional CFD model and a hybrid algorithm," Shock Waves **31**, 271 (2021).

[4]O. Abidakun, A. Adebiyi, D. Valiev, and V. y. Akkerman, "Impacts of fuel nonequidiffusivity on premixed flame propagation in channels with open ends," Physics of Fluids **33**, 013604 (2021).

[5]B. An, Z. Wang, and M. Sun, "Flame stabilization enhancement by microjet-based virtual shock wave generators in a supersonic combustor," Physics of Fluids **33**, 016104 (2021).

[6]V. Robles, E. Gutierrez-Herrera, L. F. Devia-Cruz, D. Banks, S. Camacho-Lopez, and G. Aguilar, "Soft material perforation via double-bubble laser-induced cavitation microjets," Physics of Fluids **32**, 042005 (2020).

[7]B. Sturtevant, and T. Okamura, "Dependence of shock-tube boundary layers on shock strength," The Physics of Fluids **12**, 1723 (1969).

[8]A. Roshko, "On flow duration in low-pressure shock tubes," The Physics of Fluids **3**, 835 (1960).

[9]R. Balakrishnan, "An approach to entropy consistency in second-order hydrodynamic equations," Journal of Fluid Mechanics **503**, 201 (2004).

[10]S. Paolucci, and C. Paolucci, "A second-order continuum theory of fluids," Journal of Fluid Mechanics **846**, 686 (2018).

[11]Z. Cai, and Y. Wang, "Regularized 13-moment equations for inverse power law models," Journal of Fluid Mechanics **894**, A12 (2020).

[12]R. S. Jadhav, A. Gavasane, and A. Agrawal, "Improved theory for shock waves using the OBurnett equations," Journal of Fluid Mechanics **929**, A37 (2021).

[13]W. Garen, B. Meyerer, S. Udagawa, and K. Maeno, *Shock Waves in Mini-tubes: Influence of the Scaling Parameter S* (Springer, 2009).

[14]J. Austin, and D. J. Bodony, "Wave propagation in gaseous small-scale channel flows," Shock Waves **21**, 547 (2011).

[15]G. Mirshekari, M. Brouillette, J. Giordano, C. Hébert, J.-D. Parisse, and P. Perrier, "Shock waves in microchannels," Journal of Fluid Mechanics **724**, 259 (2013).

[16]A. Mukhambetiyar, M. Jaeger, and D. Adair, "CFD modelling of flow characteristics in micro shock tubes, " Journal of Applied Fluid Mechanics **10**, 1061 (2017).

[17]Y. Kai, W. Garen, D. E. Zeitoun, and U. Teubner, "Formation and hot flow duration of micro shock flows," Physics of Fluids **30**, 072001 (2018).

[18]G. Mirshekari, and M. Brouillette, "One-dimensional model for microscale shock tube flow," Shock Waves **19**, 25 (2009).

[19]D. Ngomo, A. Chaudhuri, A. Chinnayya, and A. Hadjadj, "Numerical study of shock propagation and attenuation in narrow tubes including friction and heat losses," Computers & Fluids **39**, 1711 (2010).

[20]D. E. Zeitoun, and Y. Burtschell, "Navier–Stokes computations in micro shock tubes," Shock Waves **15**, 241 (2006).

[21]J. Parisse, J. Giordano, P. Perrier, Y. Burtschell, and I. Graur, "Numerical investigation of micro shock waves generation," Microfluidics and Nanofluidics **6**, 699 (2009).

[22]D. E. Zeitoun, Y. Burtschell, I. A. Graur, M. S. Ivanov, A. N. Kudryavtsev, and Y. A. Bondar, "Numerical simulation of shock wave propagation in microchannels using continuum and kinetic approaches," Shock Waves **19**, 307 (2009).

[23]R. A. Kumar, H. Kim, and T. Setoguchi, "Computational analysis of the wave motions in micro-shock tube flow," Proceedings of the Institution of Mechanical Engineers, Part G: Journal of Aerospace Engineering **228**, 594 (2014).

[24]D. S. Watvisave, B. P. Puranik, and U. V. Bhandarkar, "Modeling wall effects in a micro-scale shock tube using hybrid MD–DSMC algorithm," Shock Waves **26**, 477 (2016).

[25]N. T. Weissmueller, L. Marsay, H. A. Schiffter, R. C. Carlisle, C. S. Rollier, R. K. Prud'homme, and A. J. Pollard, "Alternative vaccine administration by powder injection: Needle-free dermal delivery of the glycoconjugate meningococcal group Y vaccine," PLOS ONE **12**, e0183427 (2017).

[26]A. Mohizin, and J. K. Kim, "Current engineering and clinical aspects of needle-free injectors: A review," Journal of Mechanical Science and Technology **32**, 5737 (2018).

[27]O. Ejtehadi, A. Rahimi, A. Karchani, and R. S. Myong, "Complex wave patterns in dilute gas–particle flows based on a novel discontinuous Galerkin scheme," International Journal of Multiphase Flow **104**, 125 (2018).

[28]T. G. Theofanous, V. Mitkin, and C.-H. Chang, "Shock dispersal of dilute particle clouds," Journal of Fluid Mechanics **841**, 732 (2018).

[29]G. Gai, O. Thomine, S. Kudriakov, and A. Hadjadj, "A new formulation of a spray dispersion model for particle/droplet-laden flows subjected to shock waves," Journal of Fluid Mechanics **905**, A24 (2020).

[30]R. A. Hingson, and J. G. Hughes, "Clinical studies with jet injection.*: A new method of drug administration," Anesthesia & Analgesia **26**, 221 (1947).

[31]O. Ejtehadi, and R. S. Myong, "A modal discontinuous Galerkin method for simulating dusty and granular gas flows in thermal non-equilibrium in the Eulerian framework," Journal of Computational Physics **411**, 109410 (2020).

[32]A. Rahimi, O. Ejtehadi, K. H. Lee, and R. S. Myong, "Near-field plume-surface interaction and regolith erosion and dispersal during the lunar landing," Acta Astronautica **175**, 308 (2020).

[33]O. Ejtehadi, R. S. Myong, I. Sohn, and B. J. Kim, "Full continuum approach for simulating plume-surface interaction in planetary landings," Physics of Fluids **35**, (2023).

[34]N. Quinlan, M. Kendall, B. Bellhouse, and R. Ainsworth, "Investigations of gas and particle dynamics in first generation needle-free drug delivery devices," Shock Waves **10**, 395 (2001).

[35]M. A. F. Kendall, N. J. Quinlan, S. J. Thorpe, R. W. Ainsworth, and B. J. Bellhouse, "Measurements of the gas and particle flow within a converging-diverging nozzle for high speed powdered vaccine and drug delivery," Experiments in Fluids **37**, 128 (2004).

[36]G. Zhang, Y. Z. Jin, T. Setoguchi, and H. D. Kim, "Study on drug powder acceleration in a micro shock tube," Journal of Mechanical Science and Technology **30**, 4007 (2016).

[37]Y. Liu, "Performance studies of particle acceleration for transdermal drug delivery," Medical and Biological Engineering and Computing **44**, 551 (2006).

[38]G. Zhang, I. Lee, T. Hashimoto, T. Setoguchi, and H. Kim, "Experimental study on gas-particle two-phase flows in a micro shock tube," Journal of Visualization **20**, 17 (2017).

[39]R. S. Myong, "A generalized hydrodynamic computational model for rarefied and microscale diatomic gas flows," Journal of Computational Physics **195**, 655 (2004).

[40]R. S. Myong, "A computational method for Eu's generalized hydrodynamic equations of rarefied and microscale gasdynamics," Journal of Computational Physics **168**, 47 (2001).

[41]R. S. Myong, "Thermodynamically consistent hydrodynamic computational models for high-Knudsen-number gas flows," Physics of Fluids **11**, 2788 (1999).

[42]B. C. Eu, *Kinetic Theory of Nonequilibrium Ensembles, Irreversible Thermodynamics, and Generalized Hydrodynamics: Volume 1. Nonrelativistic Theories* (Springer, 2016).

[43]B. C. Eu, and Y. G. Ohr, "Generalized hydrodynamics, bulk viscosity, and sound wave absorption and dispersion in dilute rigid molecular gases," Physics of Fluids **13**, 744 (2001).

[44]B. C. Eu, *Kinetic Theory and Irreversible Thermodynamics* (John Wiley and Sons, Inc., 1992).

[45]S. Singh, A. Karchani, and R. S. Myong, "Non-equilibrium effects of diatomic and polyatomic gases on the shock-vortex interaction based on the second-order constitutive model of the Boltzmann-Curtiss equation," Physics of Fluids **30**, 016109 (2018).

[46]T. K. Mankodi, and R. S. Myong, "Boltzmann-based second-order constitutive models of diatomic and polyatomic gases including the vibrational mode," Physics of Fluids **32**, 126109 (2020).

[47]R. Ishii, Y. Umeda, and M. Yuhi, "Numerical analysis of gas-particle two-phase flows," Journal of Fluid Mechanics **203**, 475 (1989).

[48]T. Saito, "Numerical analysis of dusty-gas flows," Journal of Computational Physics **176**, 129 (2002).

[49]O. Igra, G. Hu, J. Falcovitz, and B. Wang, "Shock wave reflection from a wedge in a dusty gas," International Journal of Multiphase Flow **30**, 1139 (2004).

[50]R. W. Houim, and E. S. Oran, "A multiphase model for compressible granular–gaseous flows: formulation and initial tests," Journal of Fluid Mechanics **789**, 166 (2016).

[51]C. B. Henderson, "Drag coefficients of spheres in continuum and rarefied flows," AIAA Journal **14**, 707 (1976).

[52]F. M. White, and I. Corfield, *Viscous Fluid Flow* (McGraw-Hill New York, 2006).

[53]T. Saito, M. Marumoto, and K. Takayama, "Numerical investigations of shock waves in gas-particle mixtures," Shock Waves **13**, 299 (2003).

[54]G. Ben-Dor, O. Igra, and L. Wang, "Shock wave reflections in dust-gas suspensions," Journal of Fluids Engineering **123**, 145 (2001).

[55]F. Dobran, A. Neri, and G. Macedonio, "Numerical simulation of collapsing volcanic columns," Journal of Geophysical Research: Solid Earth **98**, 4231 (1993).

[56]J. G. Knudsen, and D. L. Katz, *Fluid Dynamics and Heat Transfer* (New York, McGraw-Hill Book Company, 1958).

[57]C. Curtiss, "The classical Boltzmann equation of a gas of diatomic molecules," The Journal of Chemical Physics **75**, 376 (1981).

[58]R. S. Myong, "Coupled nonlinear constitutive models for rarefied and microscale gas flows: subtle interplay of kinematics and dissipation effects," Continuum Mechanics and Thermodynamics **21**, 389 (2009).

[59]R. S. Myong, "On the high Mach number shock structure singularity caused by overreach of Maxwellian molecules," Physics of Fluids **26**, 056102 (2014).

[60]L. Onsager, "Reciprocal relations in irreversible processes. I," Physical review **37**, 405 (1931).

[61]F. R. W. McCourt, J. J. M. Beenakker, W. E. Köhler, and I. Kuscer, *Nonequilibrium Phenomena in Polyatomic Gases: Dilute Gases* (Clarendon Press, 1990).

[62]M. Al-Ghoul, and B. C. Eu, "Nonequilibrium partition function in the presence of heat flow," Journal of Chemical Physics, **115(18)**, 8481 (2001).

[63]A. Koop, *Numerical Simulation of Unsteady Three-dimensional Sheet Cavitation*, (University of Twente, Ph. D. Thesis, 2008).

[64]K. G. Powell, P. L. Roe, R. S. Myong, and T. Gombosi, "An upwind scheme for magnetohydrodynamics," AIAA Paper 1995-1704 (1995).

[65]K. G. Powell, P. L. Roe, T. J. Linde, T. I. Gombosi, and D. L. De Zeeuw, "A solution-adaptive upwind scheme for ideal magnetohydrodynamics," Journal of Computational Physics **154**, 284 (1999).

[66]P. Janhunen, "A positive conservative method for magnetohydrodynamics based on HLL and Roe methods," Journal of Computational Physics **160**, 649 (2000).

[67]S. Jung, and R. S. Myong, "A second-order positivity-preserving finite volume upwind scheme for air-mixed droplet flow in atmospheric icing," Computers & Fluids **86**, 459 (2013).

[68]T. Chourushi, A. Rahimi, S. Singh, O. Ejtehadi, T. K. Mankodi, and R. S. Myong, "Thermal and flow characteristics of nonequilibrium monatomic, diatomic, and polyatomic gases in cylindrical Couette flow based on second-order non-Navier–Fourier constitutive model," International Journal of Heat and Mass Transfer **187**, 122580 (2022).

[69]Z. Yuan, W. Zhao, Z. Jiang, W. Chen, and R. K. Agarwal, "Modified nonlinear coupled constitutive relations model for hypersonic nonequilibrium flows," Journal of Thermophysics and Heat Transfer **34**, 848 (2020).

[70]Z. He, Z. Jiang, H. Zhang, and W. Chen, "Analytical method of nonlinear coupled constitutive relations for rarefied non-equilibrium flows," Chinese Journal of Aeronautics **34**, 136 (2021).

[71]Z. Yuan, W. Zhao, Z. Jiang, and W. Chen, "Numerical simulation of hypersonic reaction flows with nonlinear coupled constitutive relations," Aerospace Science and Technology **112**, 106591 (2021).

[72]W. Zhao, L. Jiang, S. Yao, and W. Chen, "Data-driven nonlinear constitutive relations for rarefied flow computations," Advances in Aerodynamics **3**, 30 (2021).

[73]J. C. Maxwell, "VII. On stresses in rarified gases arising from inequalities of temperature," Philosophical Transactions of the Royal Society of London 231 (1879).

[74]M. Smoluchowski von Smolan, "Ueber wärmeleitung in verdünnten gasen," Annalen der Physik **300**, 101 (1898).

[75]S. Singh, A. Karchani, T. Chourushi, and R. S. Myong, "A three-dimensional modal discontinuous Galerkin method for the second-order Boltzmann-Curtiss-based constitutive model of rarefied and microscale gas flows," Journal of Computational Physics **457**, 111052 (2022).

[76]S. Zeng, W. Zhao, Z. Jiang, W. Chen, "A second-order slip/jump boundary condition modified by nonlinear Rayleigh–Onsager dissipation factor," Physics of Fluids **35**, 042001 (2023).

[77]O. Ejtehadi, E. Roohi, and J. A. Esfahani, "Investigation of basic molecular gas structural effects on hydrodynamics and thermal behaviors of rarefied shear driven micro/nano flow using DSMC," International Communications in Heat and Mass Transfer **39**, 439 (2012).

[78]O. Ejtehadi, E. Roohi, and J. A. Esfahani, "Detailed investigation of hydrodynamics and thermal behavior of nano/micro shear driven flow using DSMC," Scientia Iranica. Transaction B, Mechanical Engineering **20**, 1228 (2013).

[79]J. A. Esfahani, O. Ejtehadi, and E. Roohi, "Second law analysis of micro/nano Couette flow using direct simulation Monte Carlo method," International Journal of Exergy **13**, 320 (2013).

[80]R. S. Myong, A. Karchani, and O. Ejtehadi, "A review and perspective on a convergence analysis of the direct simulation Monte Carlo and solution verification," Physics of Fluids **31**, 066101 (2019).

[81]S. Singh, A. Karchani, K. Sharma, and R. S. Myong, "Topology of the second-order constitutive model based on the Boltzmann–Curtiss kinetic equation for diatomic and polyatomic gases," Physics of Fluids **32**, 026104 (2020).

[82]B. Sharma, R. Kumar, P. Gupta, S. Pareek, A. Singh, "On the estimation of bulk viscosity of dilute nitrogen gas using equilibrium molecular dynamics approach," Physics of Fluids **34**, 057104 (2022).

[83]Z. Yuan, Z. Jiang, W. Zhao, and W. Chen, "Multiple temperature model of nonlinear coupled constitutive relations for hypersonic diatomic gas flows," AIP Advances **10**, (2020).

[84]S. Kosuge, and K. Aoki, "Shock-wave structure for a polyatomic gas with large bulk viscosity," Physical Review Fluids **3**, 023401 (2018).

[85]S. Taniguchi, T. Arima, T. Ruggeri, and M. Sugiyama, "Overshoot of the non-equilibrium temperature in the shock wave structure of a rarefied polyatomic gas subject to the dynamic pressure," International Journal of Non-Linear Mechanics **79**, 66 (2016).

[86]C. T. Crowe, *Multiphase Flow Handbook* (CRC Press, 2005).

[87]L. P. Raj, K. Yee, and R. S. Myong, "Sensitivity of ice accretion and aerodynamic performance degradation to critical physical and modeling parameters affecting airfoil icing," Aerospace Science and Technology **98**, 105659 (2020).

[88]S. Singh, M. Battiato, and R. S. Myong, “Impact of bulk viscosity on flow morphology of shock-accelerated cylindrical light bubble in diatomic and polyatomic gases,” Physics of Fluids **33**, 066103 (2021).